



# Development of On-Chip Multi-Imaging Flow Cytometry for Identification of Imaging Biomarkers of Clustered Circulating Tumor Cells

Hyonchol Kim<sup>1</sup>, Hideyuki Terazono<sup>1,2</sup>, Yoshiyasu Nakamura<sup>3</sup>, Kazuko Sakai<sup>4</sup>, Akihiro Hattori<sup>1</sup>, Masao Odaka<sup>1</sup>, Mathias Girault<sup>1</sup>, Tokuzo Arao<sup>4</sup>, Kazuto Nishio<sup>4</sup>, Yohei Miyagi<sup>3</sup>, Kenji Yasuda<sup>1,2\*</sup>

**1** Kanagawa Academy of Science and Technology, Takatsu, Kawasaki, Japan, **2** Department of Biomedical Information, Division of Biosystems, Institute of Biomaterials and Bioengineering, Tokyo Medical and Dental University, Chiyoda, Tokyo, Japan, **3** Molecular Pathology and Genetics Division, Kanagawa Cancer Center Research Institute, Asahi-ku, Yokohama, Japan, **4** Department of Genome Biology, School of Medicine, Kinki University, Osaka-Sayama, Osaka, Japan

## Abstract

An on-chip multi-imaging flow cytometry system has been developed to obtain morphometric parameters of cell clusters such as cell number, perimeter, total cross-sectional area, number of nuclei and size of clusters as “imaging biomarkers”, with simultaneous acquisition and analysis of both bright-field (BF) and fluorescent (FL) images at 200 frames per second (fps); by using this system, we examined the effectiveness of using imaging biomarkers for the identification of clustered circulating tumor cells (CTCs). Sample blood of rats in which a prostate cancer cell line (MAT-LyLu) had been pre-implanted was applied to a microchannel on a disposable microchip after staining the nuclei using fluorescent dye for their visualization, and the acquired images were measured and compared with those of healthy rats. In terms of the results, clustered cells having (1) cell area larger than 200  $\mu\text{m}^2$  and (2) nucleus area larger than 90  $\mu\text{m}^2$  were specifically observed in cancer cell-implanted blood, but were not observed in healthy rats. In addition, (3) clusters having more than 3 nuclei were specific for cancer-implanted blood and (4) a ratio between the actual perimeter and the perimeter calculated from the obtained area, which reflects a shape distorted from ideal roundness, of less than 0.90 was specific for all clusters having more than 3 nuclei and was also specific for cancer-implanted blood. The collected clusters larger than 300  $\mu\text{m}^2$  were examined by quantitative gene copy number assay, and were identified as being CTCs. These results indicate the usefulness of the imaging biomarkers for characterizing clusters, and all of the four examined imaging biomarkers—cluster area, nuclei area, nuclei number, and ratio of perimeter—can identify clustered CTCs in blood with the same level of preciseness using multi-imaging cytometry.

Citation: Kim H, Terazono H, Nakamura Y, Sakai K, Hattori A, et al. (2014) Development of On-Chip Multi-Imaging Flow Cytometry for Identification of Imaging Biomarkers of Clustered Circulating Tumor Cells. PLoS ONE 9(8): e104372. doi:10.1371/journal.pone.0104372

Editor: Thomas Dittmar, Witten/Herdecke University, Germany

Received January 30, 2014; Accepted July 10, 2014; Published August 20, 2014

Copyright: © 2014 Kim et al. This is an open-access article distributed under the terms of the Creative Commons Attribution License, which permits unrestricted use, distribution, and reproduction in any medium, provided the original author and source are credited.

Funding: This work was supported by Kanagawa Prefector's local basic science funding for the On-chip Cellomics Project at the Kanagawa Academy of Science and Technology. The funder had no role in study design, data collection and analysis, decision to publish, or preparation of the manuscript.

Competing Interests: The authors have declared that no competing interests exist.

\* Email: yasuda.bmi@tmd.ac.jp

## Introduction

Finding irregular cells in blood is fundamental to achieving non-invasive health checks, such as cancer and immune diagnostics. For example, circulating tumor cells (CTCs) are expected to form additional seeds for subsequent growth of tumors [1–3], and quantitative detection of CTCs in the blood [4–8] has the potential to achieve minimally invasive cancer diagnosis in comparison with conventional biopsies. One major approach to finding irregular cells is the targeting of specific molecules, molecular biomarkers, on the cell surface [1,3,6,9,10]; however, its application has sometimes had the difficulty of false-negative detection because of the variety of molecular expression properties of targeted cells.

To overcome these difficulties, we developed another system for the recognition of target cells [11–13]. In this system, cell samples were applied to a microchannel fabricated on a small microchip, cellular images were taken with a high-speed CCD camera, and target cells were identified depending on their morphological

characteristics, such as cellular area and perimeter. These morphological parameters, referred to as “imaging biomarkers” hereafter, are other indexes to identify specific target cells. For example, a large cellular size was indicated for some tumor cells [14–17], and a larger nucleus than in healthy cells is known as one common property of the morphometric phenotype of cancer cells [18–24]; therefore, finding target cells using imaging biomarkers, especially using both cell size and nucleus conformation, is useful for the identification of tumor cells. In this study, a real-time cell sorting system to achieve simultaneous processing of imaging biomarkers for both optical image (i.e., total cell configuration) and fluorescent image (i.e., nucleus configuration) was developed, and it was applied to identify irregular cells, especially clustered cells, in a blood sample. According to previous reports on CTC detection, the possibility of the CTCs forming clusters was suggested [7]; however, clear evidence had not been identified and there have been no quantitative studies on the identification of clustered cells in the blood. Here, a quantitative approach for cluster detection was suggested using imaging biomarkers as detection indexes.

## Materials and Methods

### Fabrication of microchip

The microchip was fabricated by the following procedure. A mask blank, which was a glass substrate coated with both chromium for light interception and positive photo-resist (AZP1350) for the fabrication of patterns (CBL4006Du-AZP, Clean Surface Technology Co., Kanagawa, Japan), was set to a laser lithography system (DDB-3TH, Neoark, Co., Tokyo, Japan) and a laser (405 nm wavelength) was irradiated onto the mask blank in the same pattern as the microchannel used in this study. After the irradiation, the mask blank was immersed in a developer of the resist (NMD-3, Tokyo Ohka Kogyo Co., Kanagawa, Japan) to remove the resist on which the laser was irradiated; then, a chromium layer was bared at this position. Next, the mask blank was immersed in chromium etching solution (MPM-E350, DNP Fine Chemicals, Co., Kanagawa, Japan), after which the bared chromium layer was removed and a transparent pattern of the microchannel was formed on the substrate. Finally, the whole resist on the mask blank was removed by light irradiation onto the whole of the substrate and immersion of the substrate in the developer; then, a photo mask of the microchannel was fabricated.

On the other hand, a light-curing resin (SU-8 3025, Nippon Kayaku Co., Tokyo, Japan) was spin-coated using a spin coater (1H-DX2, Mikasa, Co., Tokyo, Japan) of 25 mm thickness on a clean Si substrate. The resin-coated substrate was pre-baked at 95°C for 15 min, set in a mask aligner with the fabricated photo mask (MA-20, Mikasa), and the light (365 nm wavelength) was irradiated through the mask to harden the resin with the pattern of the microchannel. The substrate was heated at 65°C for 1 min and 95°C for 5 min sequentially to promote hardening of the resin, and excess resin was removed by immersing the substrate in SU-8 developer (Nippon Kayaku). A mold of the microchannel was then fabricated using the resin on the Si substrate.

To fabricate the chip, poly(dimethylsiloxane) (PDMS; SYLGARD 184 silicon elastomer, Dow Corning Co., Midland, MI, USA) was dropped onto the fabricated mold in sol state, and heated at 90°C for 1 h to harden the PDMS. The PDMS on which the pattern of the microchannel was transferred was peeled off from the mold and stuck with cleaned cover glass. Finally, plastic columns for the application of solvents including sample blood were pasted on the PDMS with epoxy resin; then, the microchip to be used in this study was fabricated.

### Preparation of sample blood

This study was carried out in strict accordance with the Act on Welfare and Management of Animals of the Ministry of the Environment, Japan. The protocol was approved by the animal experiment committee of the Kanagawa Cancer Center (permit number 21-02). MAT-LyLu is a rat prostate cancer cell line established from the original Dunning R3327 tumor maintained by *in vivo* passage of a prostate cancer that spontaneously occurred in a Copenhagen rat [25]. This cell line was a generous gift from the original founders through Hisao Ekimoto, Ph.D., at the Oncology Section, Laboratory of Biology, Nippon Kayaku Co., Ltd., and was maintained in our laboratory.

To obtain blood containing cancer cells, the MAT-LyLu was adjusted to  $5 \times 10^6$  cells in 200 mL of cell culture medium (RPMI 1640, Life Technologies Co., Grand Island, NY, USA), and implanted into the dorsal subcutaneous tissue of a Copenhagen rat (male, 6 weeks old). At 2 weeks after implantation, blood of the rat was collected from the subclavian vein using a collection tube containing heparin. The blood was hemolyzed using commercial reagent (BD Pharm Lyse, without fixative, BD Biosciences, San

Jose, CA, USA) for 10 min, washed along with 2006 g centrifugation for 5 min and re-suspended two times in phosphate-buffered saline (PBS) containing 1% bovine serum albumin, suspended in PBS containing 100 ng/mL Hoechst 33258, and then incubated for 10 min to stain cellular nuclei. The sample was washed again along with centrifugation 3 times, suspended in 5% glucose solution, and applied to the sample inlet on the chip.

### Flow cytometry

The prepared sample blood was applied to the sample inlet on a fabricated microchip with a sample volume of 50  $\mu$ L in an assay. The same buffer with the sample cell suspension (i.e., 5% glucose) was also used as a sheath buffer, and was applied to the sheath buffer inlet. Air pressure was applied onto both sample and sheath buffer inlets simultaneously using a syringe pump to introduce these liquids into the microchannels. Before starting the experiments, flow velocity was calibrated by taking images of calibration beads using a CCD camera (Ditect Co., Tokyo, Japan) as the shift of bead position in the microchannel within a few frames of the images, and typically, 1 kPa pressure achieved flow velocity of about 3 mm/sec at the position after the meeting of sample and sheath flows. Multi-imaging observations of sample blood were then performed through the multi-view unit with 3 mm/sec flow velocity and 200 fps acquisition rate.

### Comparative genomic hybridization analysis

Rat genome comparative genomic hybridization (CGH) microarray 244A (Agilent Technologies, Santa Clara, CA, USA) was used to perform array CGH on genomic DNA obtained from the MAT-LyLu cell line according to the manufacturer's instructions. A DNA sample obtained from liver tissue of a healthy Copenhagen rat was used as a reference. Genomic DNAs were extracted using a QIAamp DNA Mini kit (Qiagen, Hilden, Germany) according to the manufacturer's instructions. The DNA concentration was determined with PicoGreen dsDNA Quantitation Reagent (Life Technologies). Agilent Genomic Workbench (Agilent Technologies) was used to analyze chromosomal patterns using an ADM-2 algorithm setting a threshold of 5.0.

### Copy number assay

The gene copy numbers for *csrp2* and *zdhhc17* were determined using TaqMan Copy Number Assays according to the manufacturer's instructions (Applied Biosystems, Foster City, CA, USA). The gene-specific primers and TaqMan probes were used in the experiments had the following sequences. Rat *csrp2* primers were: sense, 5'-GGACTAAATGGATTGATGCCACTCT-3'; antisense, 5'-GTCCCTGCTTCAAAGAACTGTCT-3'; probe, 5'-FAM-AAGAGCAAGAAAGGAAACCC-MGB-NFQ-3'. Rat *zdhhc17* primers were: sense, 5'-GCCCTACTGCATGATGATACA-3'; antisense, 5'-GGGCTGTTTTGCATGAAATTCATCA-3'; probe, 5'-FAM-CTGGACAGCATCTGCTAGTATAC-MGB-NFQ-3'. Rat *rpp40* primers were: sense, 5'-GTATGACACTGGCATGGAAGTCT-3'; antisense, 5'-CT-TGCAGTCTCTGTGGAT-3'; probe, 5'-FAM-CCTGGC-AATCAAAGTTAGGCTTAG-MGB-NFQ-3'. Genomic DNAs obtained from collected samples using the cell sorting system were extracted using a QIAamp DNA Micro kit (Qiagen) according to the manufacturer's instructions. The DNA concentrations were determined with PicoGreen dsDNA Quantitation Reagent. Rat *rpp40* was used as an internal control. Genomic DNAs obtained from MAT-LyLu cell line and healthy rat liver were used as positive and negative controls, respectively.

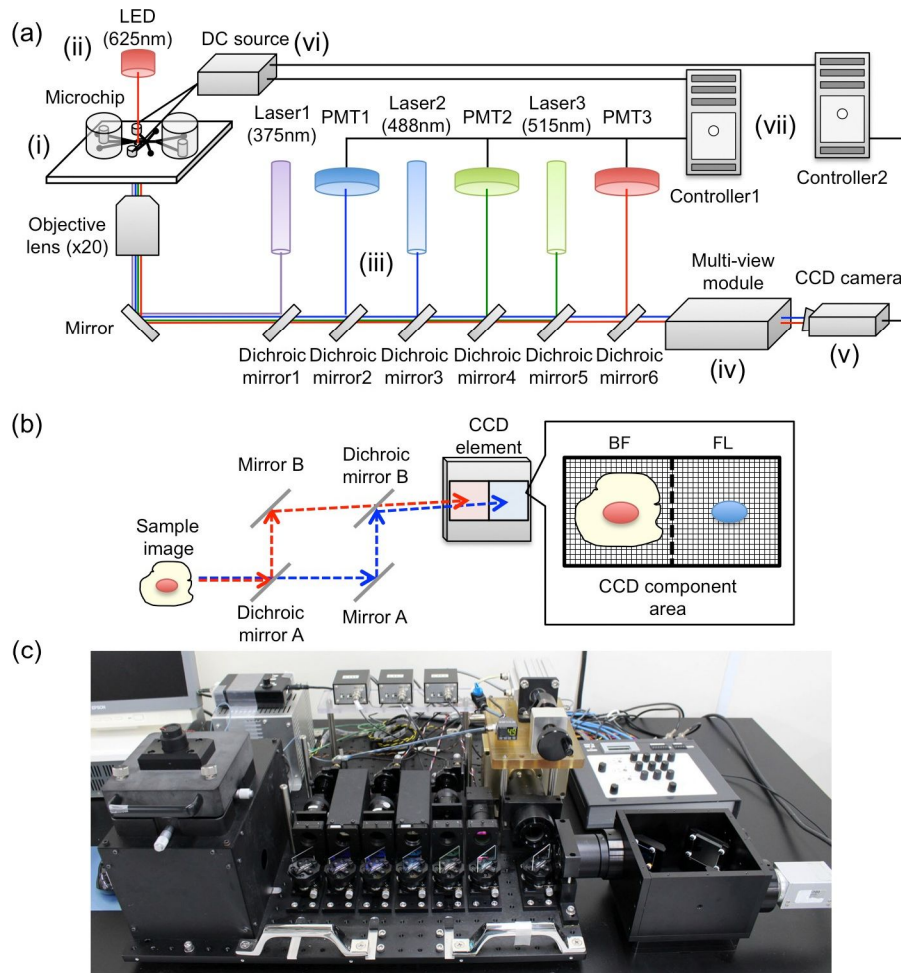


Figure 1. Instrumental set-up. (a) Summary of the on-chip multi-imaging flow cytometry system. The system was composed of seven major modules: (i) microchip, (ii) bright-field (BF) imaging, (iii) fluorescent (FL) detection, (iv) multi-view, (v) CCD camera, (vi) sorting, and (vii) controller, as numbered in the figure. (b) Summary of the multi-view module. (c) A photograph of the system. doi:10.1371/journal.pone.0104372.g001

**Results**

**Development of on-chip multi-imaging flow cytometry system**

The on-chip multi-imaging flow cytometry system (Fig. 1) was composed of seven major modules as an improvement of previous systems [11–13,26]: (i) microchip, (ii) bright-field (BF) light source, (iii) fluorescent (FL) excitation and detection, (iv) multi-view, (v) CCD camera, (vi) sorting, and (vii) controller, as numbered in Fig. 1 (a). In the BF light source module, an LED (625 nm wavelength) was used as a source for taking BF images and was irradiated from the top of the chip. This allowed simultaneous measurements of both BF and FL images, avoiding interference of the wavelengths during the measurements. An objective lens having 206 magnification and a 0.75 numerical aperture was set to the system, which allowed clear cell images to be taken within the depth range of the microchannel (25 μm) [27]. The FL excitation and detection modules contained three excitation lasers (375, 488, and 515 nm) and photomultipliers (PMTs), respectively, to monitor three different FL signals, which allowed conventional FL detection with labeling of target biomarkers. The controller module consisted of two independent units: one calculated FL signals and the other processed imaging biomarkers in multi-view

images. Maximum frequencies of calculations were 10,000 frequencies per second (fps) for controller 1, which calculated FL intensities, and 200 fps for controller 2, which processed imaging biomarkers for the current system. According to the adjustment of suitable thresholds for these parameters, feedback signals could be sent to the sorting module. The sorting module was composed of a direct current (DC) source and electrodes connected with a microchip, and could apply DC voltages to cells flowing in a microchannel of the chip to purify target cells under feedback signals, if necessary. Figure 1 (b) shows the principle of the multi-view module [27,28] used in this study. Firstly, optical paths between BF (red) and FL (blue) lights were separated using dichroic mirror A, as indicated in the figure. Next, angles of mirrors A and B were adjusted; then, BF and FL images were projected onto each half of a CCD component in the camera. An overview of the total system is shown in Fig. 1 (c). The system has a desktop size of 60 cm × 60 cm.

Figure 2 shows the microchip designed to be suitable for this study. The chip body was fabricated with poly(dimethylsiloxane) (PDMS) attached to a cover glass to apply optical transparency in the observation. Microchannels were placed between the PDMS and the bottom cover glass in the chip with a 2 mmQ buffer entrance penetrating the PDMS. The upper stream of the

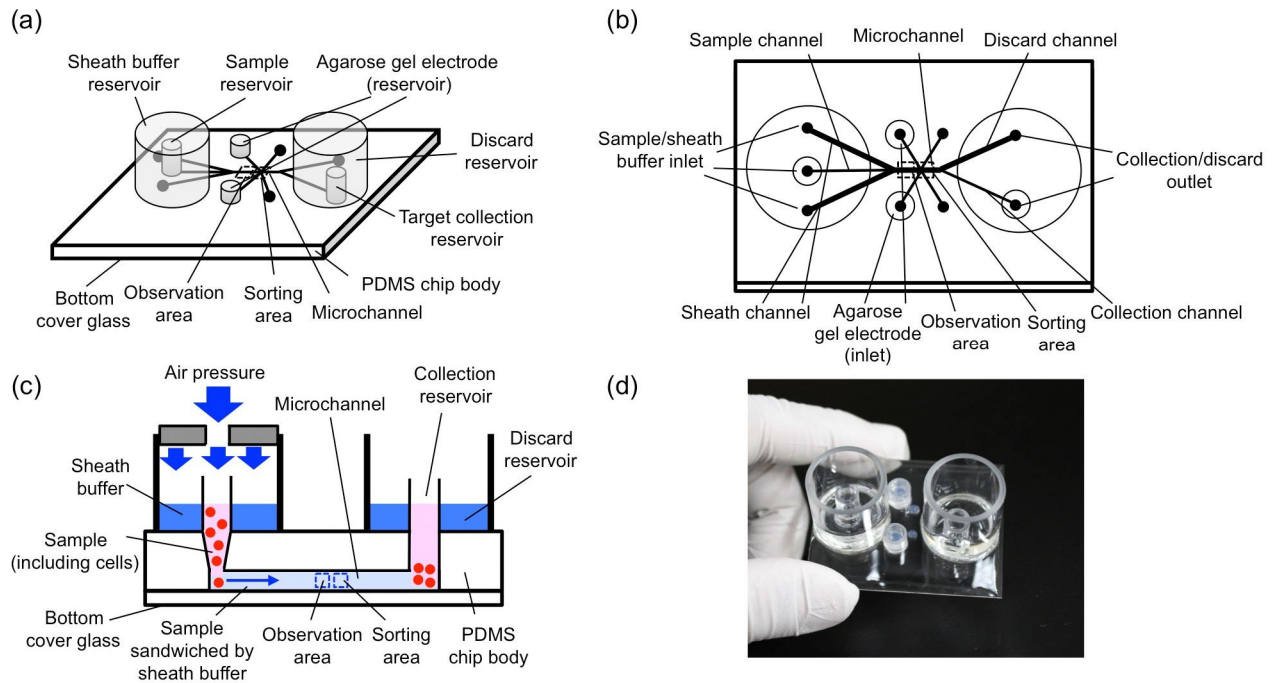


Figure 2. Overview of the microchip. (a) Diagonal, (b) top, and (c) side views of the microchip used in this study. (d) A photograph of the chip. Total chip size is 50 mm × 40 mm. doi:10.1371/journal.pone.0104372.g002

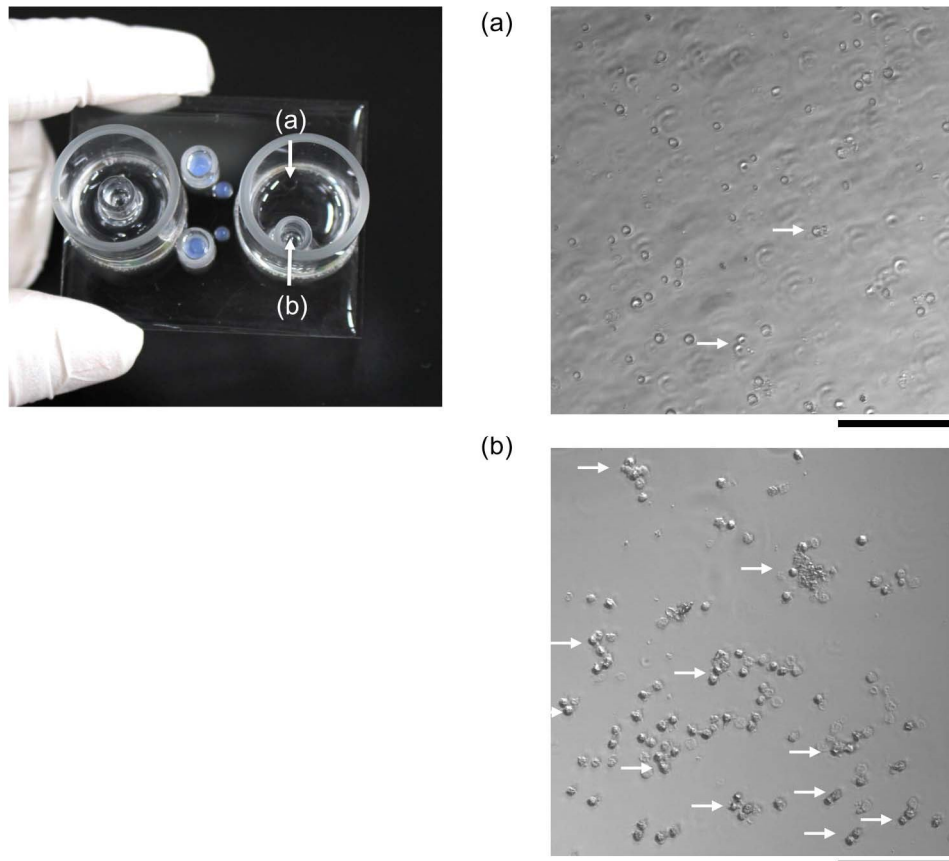


Figure 3. An example of cell sorting. Two photographs of the discarded reservoir (a) and the collection reservoir (b) indicated in the chip photograph are shown. Clustered cells are indicated by white arrows. Bars, 100 μm. doi:10.1371/journal.pone.0104372.g003

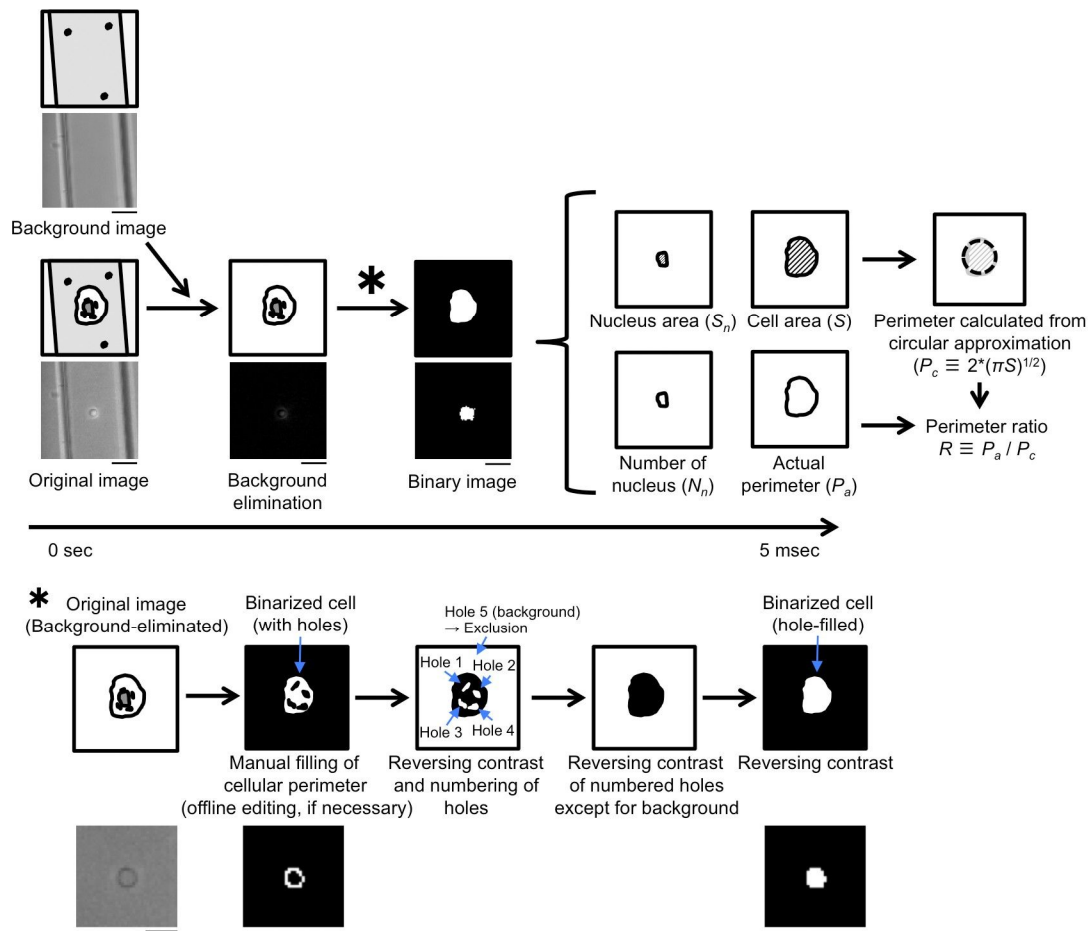


Figure 4. Summary of image processing. Firstly, photographs of both a cell and the background were taken. Next, the background image was subtracted from the cell image and holes were filled. Finally, imaging biomarkers,  $S$ ,  $S_n$ ,  $N_n$ , and  $R$ , were calculated. Bars, 10  $\mu\text{m}$ . The hole-filling procedure is explained as indicated by an asterisk. Bar, 10  $\mu\text{m}$ . doi:10.1371/journal.pone.0104372.g004

microchannel was branched into three channels: the center connected with the sample inlet and the others were a sheath buffer inlet. Both sample and sheath buffers were introduced into the channel with application of air pressure onto both sample and sheath buffer inlets, simultaneously (Fig. 2 (c)). After the meeting of sample and sheath flows, the width of the sample flow was focused in the central one-third, which allowed imaging of each single cell upon the arrangement of all the cells in a straight line.

Images of the linearly arranged cells were obtained through the multi-view module and processed by the system (see Fig. 1), and when a target cell was found, DC voltage (typically 40 V with 100 msec length) was applied to the cell through the agarose gel electrode (Fig. 2 (a) and (b)) to change its course in the collection channel [11,13]. Figure 3 shows a typical example of the cell sorting with a blood sample of a cancer-implanted rat. As shown in this figure, target cells were set into cell clusters having a large BF area, and once the value of the BF area of the observed cell exceeded the pre-adjusted threshold value, 300  $\mu\text{m}^2$  in this model case, a sorting voltage was applied to the cell and, finally, target cells were collected into the target collection reservoir. Figures 3 (a) and (b) show pictures taken for discarding (a) and collection (b) reservoirs, respectively. As shown in Fig. 3 (b), large cell clusters (indicated by arrows in the figures) were collected into the collection reservoir. On the other hand, single cells or small cell clusters were collected into the discarding reservoir (Fig. 3 (a)),

indicating the success of target collection using one imaging biomarker, BF area, as a collection parameter. The sorting capacity, which has been determined as the ratio between the number of target cells automatically detected by the system and the actual number of cells in the collection reservoir, was 24%. The low capacity of target cell collection was caused by the higher threshold setting in both recognition and collection processes to prevent 'false positive' sample collection. When the commercially available microbeads were used as a model target in this system, sorting capacity increased to 91%.

As shown in Fig. 3, target cells can be recognized by comparison of the imaging biomarkers with the threshold values pre-adjusted in the system. Figure 4 shows the detail of image processing in the system to obtain imaging biomarkers. Firstly, a background image, which was taken before the assay of flow cytometry, was subtracted from the obtained image with reductions of 8-bit grayscale values in each pixel. Next, the subtracted image was transformed to a binary image using a suitable threshold and pixel errors in the cell, which appeared by almost the same contrast in the cell as in the background, were filled (Fig. 4, asterisk); then, an extracted cell image was obtained. Finally, imaging biomarkers were calculated from the extracted cell image. In the current system, cell area ( $S$ ) and actual perimeter ( $P_a$ ) were obtained from the BF image, and nucleus area ( $S_n$ ) and number of nuclei ( $N_n$ ) were obtained from the FL image.

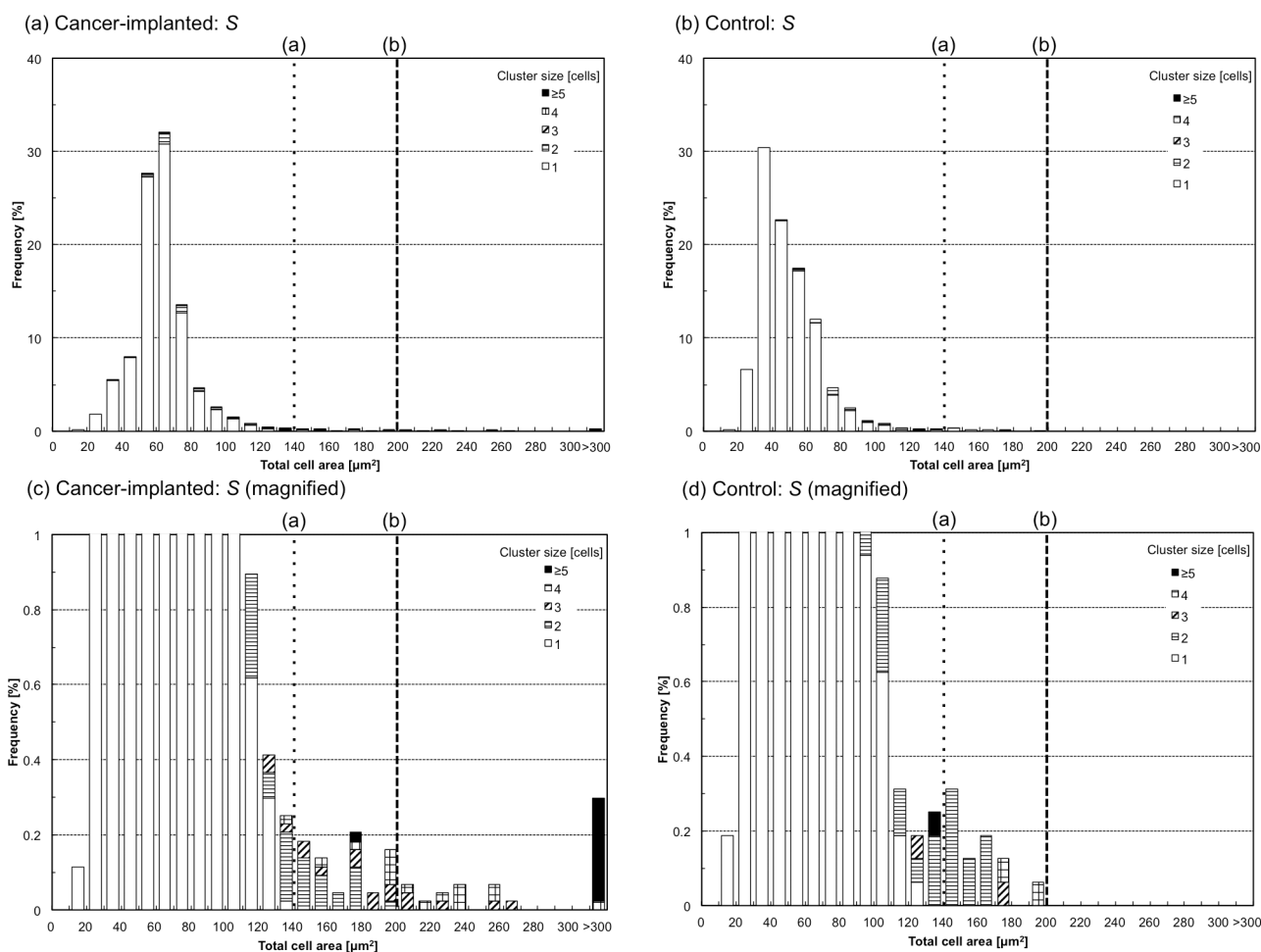


Figure 5. Histograms of total cell area, S, for cancer cell-implanted (a and c) and control blood (b and d). Two threshold values (a) and (b) for cluster identifications are indicated as dotted and dashed lines. doi:10.1371/journal.pone.0104372.g005

Additionally, the perimeter ratio, R, which was obtained as the ratio between  $P_a$  and the perimeter calculated from S ( $P_c$ ) [29], was also obtained. These calculations were performed in real time at 200 fps using controller 2 in Fig. 1, and in this study, manual calculations of the imaging biomarkers, including a few modifications for apparently failed auto-calculations caused by the failure of continuous detection of the cell perimeter in the hole filling procedure, were also performed as post-processing to confirm the reliabilities of the obtained imaging biomarker values.

### Detection of clustered cells in cancer-implanted rat blood using imaging biomarkers

After the success of the system development, its performance for the identification of specific target cells using imaging biomarkers was quantitatively evaluated. Blood of a rat in which a rat prostate cancer cell line (MAT-LyLu) had been implanted was chosen as a model sample, and clustered cells in the blood were set as a target for the detection using imaging biomarkers with the developed system. One approach anticipated to achieve successful detection of the clusters is the use of cell area; therefore, areas in BF images (i.e., total cell area, S) and FL images (i.e., total nucleus area,  $S_n$ ) were measured using the system. Figures 5 and 6 are histograms of S (Fig. 5) and  $S_n$  (Fig. 6) for cells in the cancer-implanted blood (N = 4375), shown with healthy rat blood as its control (N = 1599).

Detailed numbers including S and  $S_n$  are also summarized in Table 1. From the results, clustered cells were observed at a count of 237 in cancer-implanted samples (5.4% of the total) and a count of 56 in the control (3.5% of the total). In addition, two clear threshold values were found in both S and  $S_n$ ; that is, (a) all cells having S larger than 140  $\mu\text{m}^2$  (count of 61, 1.4% of the total, for cancer-implanted samples and 13, 0.8% of the total, for the control) and  $S_n$  larger than 80  $\mu\text{m}^2$  (count of 34, 0.8% of the total, for cancer-implanted samples and 1, 0.1% of the total, for the control) were clustered cells, as indicated by the dotted lines in Figs. 5 and 6, and (b) the clustered cells having S larger than 200  $\mu\text{m}^2$  (count of 27, 0.6% of the total) and  $S_n$  larger than 90  $\mu\text{m}^2$  (count of 26, 0.6% of the total) were specifically observed in cancer cell-implanted blood. These results indicate that some cell clusters can be identified by using S and  $S_n$  (61 of 237, 26% of all clusters, for S and 34 of 237, 14% of all clusters, for  $S_n$ ) as parameters for detection.

Obtained pictures were manually analyzed one by one with measured values of S and  $S_n$ . Figure 7 shows examples of single- and double-cell images having one, two, or three nuclei obtained from cancer-implanted and control blood, respectively. As shown in Fig. 7, the following 3 results were obtained: (i) single cells having multiple nuclei numbering more than two were specifically included in the cancer cell-implanted blood (count of 133, 3.2% of total single cells in cancer-implanted samples), (ii) two-cell clusters

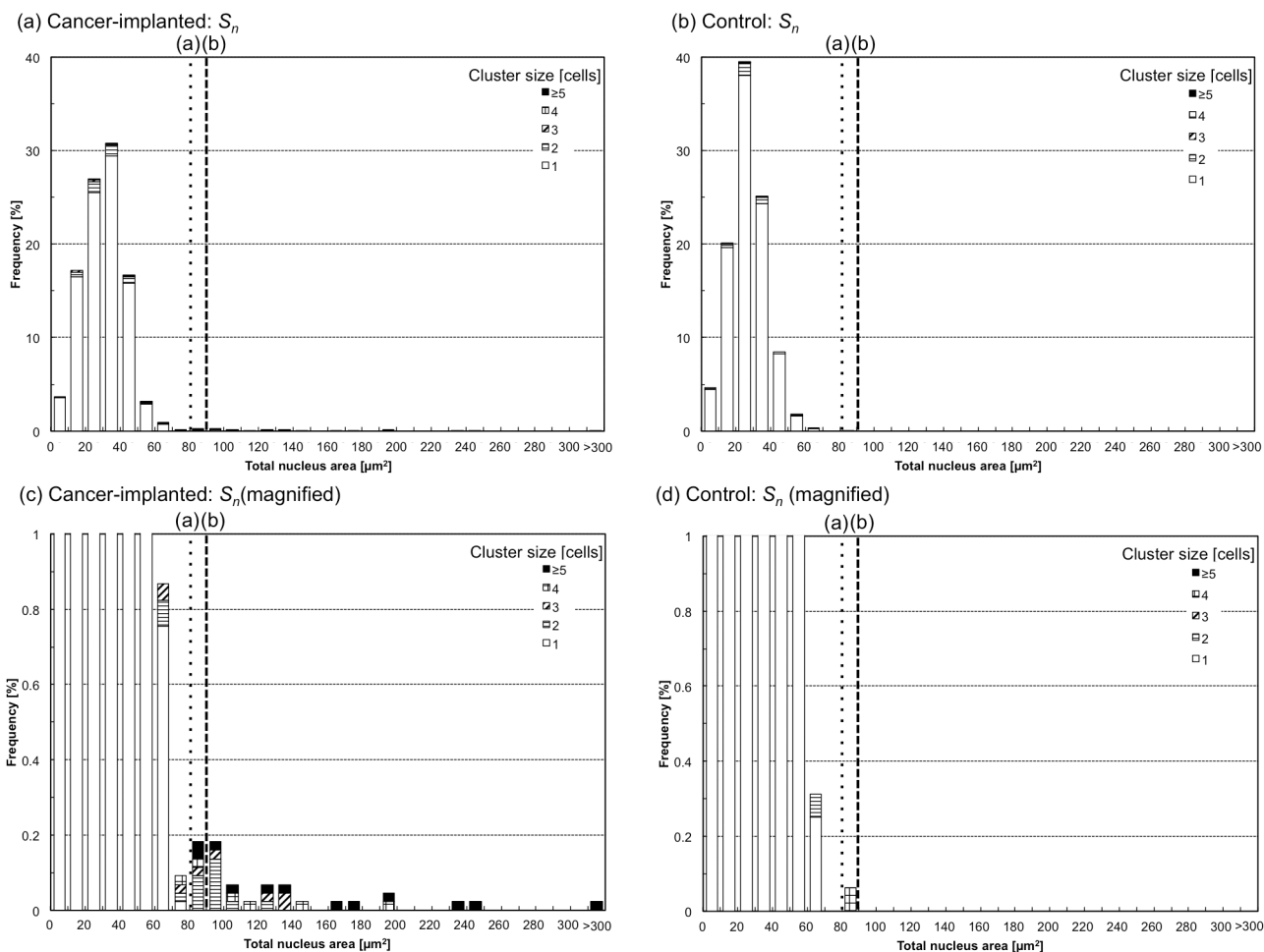


Figure 6. Histograms of total nucleus area,  $S_n$ , for cancer cell-implanted (a and c) and control blood (b and d). Two threshold values (a) and (b) for cluster identifications are indicated as dotted and dashed lines. doi:10.1371/journal.pone.0104372.g006

having only one nucleus seemed to be single cells to which a small particle (possibly debris of a hemolyzed red cell) was attached (count of 126, 72% of total two-cell clusters in cancer-implanted samples and count of 41, 84% of total two-cell clusters in control), and (iii) two-cell clusters having two nuclei were either true clusters or two independent cells flowing alongside each other (count of 48, including 2 clusters having 3 nuclei caused by the inclusion of a cell with multiple nuclei, 28% of total two-cell clusters in cancer-implanted samples and count of 8, 16% of total two-cell clusters in control). The first of these results shows the potential for the detection of implanted cancer cells having multiple nuclei, and the second can be thought of as single cells in general. The third in principle makes it difficult to distinguish two-cell clusters from two single cells using pictures; therefore, such two-cell ‘clusters’ were also contained in control blood.

Figure 8 shows typical clustered cells composed of more than 3 cells. As shown in the figure and also in Table 1, a few clusters composed of more than 3 cells were also detected in control blood (count of 7 in total), with the maximum cell number of 6. However, they seemed to be single or two independent cells to which small particles were attached (i.e., the same as result (ii) in Fig. 7), which could also be confirmed by the number of nuclei,  $N_n$ , in the cluster, which had a maximum of 2. On the other hand, clusters contained in cancer-implanted blood were composed of more than 3 cells, with 15 cells at maximum, which was also

confirmed by  $N_n$  in the cluster being more than 3. It is unlikely for more than 3 cells to be flowing alongside each other; therefore, we concluded that clusters composed of more than 3 cells containing more than 3 nuclei were truly clustered cells in the blood. Such large clusters were contained in cancer cell-implanted blood at a count of 33 (7 counts, 21% of 3-cell clusters, 12 counts, 75% of 4-cell clusters, 14 counts, 100% of 5-cell clusters, and 0.8% of the total). Measured values of  $N_n$  are summarized in Fig. 9 (a) (and also in Table 1). As shown in this figure, more than 99% of images in control blood had a single nucleus, and cell clusters having more than 3 nuclei were not contained in the blood. Figure 9 (b) also shows  $N_n$  summarized from the perspective of cluster size. As shown in the figure, large clusters in cancer-implanted blood had many nuclei, typically more than 3, indicating the possibility of the cluster formation of CTCs in the blood.

As shown in the above results,  $N_n$  is one useful imaging biomarker to identify cell clusters in blood; however, only using this marker for identification is insufficient because single cells having multiple nuclei were also contained in cancer cell-implanted blood, as shown in Fig. 7; therefore, we evaluated another imaging biomarker, perimeter ratio ( $R$ ), for the identification of clustered cells.  $R$  is defined as the ratio between the actual perimeter obtained from the cell image and the perimeter calculated with a circle approximation of  $S$ . A low value of  $R$  indicates distorted conformation of the cell away from a circular

Table 1. Summary of total cell area, S, total nucleus area, S<sub>n</sub>, number of nuclei, N<sub>n</sub>, and perimeter ratio, R, for each cluster size.

Cancer-implanted (N = 4375)			Total cell area, S [mm <sup>2</sup> ]					Total nucleus area, S <sub>n</sub> [mm <sup>2</sup> ]				
Cluster [cells]	Frequency [counts]	Frequency [%]	Average	Median	S.D.	Max.	Min.	Average	Median	S.D.	Max	Min
1	4138	94.58	62	62	15	133	11	30	31	12	73	7
2	174	3.98	88	75	33	194	36	36	33	19	122	10
3	33	0.75	133	124	58	263	53	45	33	35	134	12
4	16	0.37	219	208	57	393	136	74	52	46	195	24
\$5	14	0.32	515	421	180	1163	179	149	131	85	342	37
\$2	237	5.4	129	81	130	1163	36	47	35	41	342	10
Cancer-implanted (continued)			Number of nuclei, N <sub>n</sub>					Perimeter ratio, R				
Cluster [cells]	Frequency [counts]	Frequency [%]	Average	Median	S.D.	Max.	Min.	Average	Median	S.D.	Max	Min
1	4138	94.58	1.03	1.00	0.20	3	1	0.96	0.96	0.02	1.00	0.90
2	174	3.98	1.30	1.00	0.50	3	1	0.89	0.91	0.05	0.97	0.76
3	33	0.75	1.82	2.00	0.88	4	1	0.83	0.82	0.06	0.95	0.67
4	16	0.37	2.75	3.00	1.13	4	1	0.84	0.84	0.07	0.95	0.74
\$5	14	0.32	5.00	5.00	1.15	10	2	0.80	0.80	0.03	0.89	0.79
\$2	237	5.4	1.70	1.00	1.26	10	1	0.87	0.89	0.06	0.97	0.67
Control (N = 1599)			Total cell area, S [mm <sup>2</sup> ]					Total nucleus area, S <sub>n</sub> [mm <sup>2</sup> ]				
Cluster [cells]	Frequency [counts]	Frequency [%]	Average	Median	S.D.	Max.	Min.	Average	Median	S.D.	Max	Min
1	1543	96.50	48	44	16	121	11	27	26	10	69	7
2	49	3.06	99	83	36	169	40	28	28	12	61	7
3	3	0.19	119	127	62	177	54	23	24	10	32	13
4	2	0.13	187	187	14	197	177	51	51	43	81	20
\$5	2	0.13	116	116	24	133	99	32	44	18	57	32
\$2	56	3.5	104	88	39	197	40	29	28	14	81	7
Control (continued)			Number of nuclei, N <sub>n</sub>					Perimeter ratio, R				
Cluster [cells]	Frequency [counts]	Frequency [%]	Average	Median	S.D.	Max.	Min.	Average	Median	S.D.	Max	Min
1	1543	96.50	1.00	1.00	0.00	1	1	0.96	0.96	0.02	1.00	0.90
2	49	3.06	1.16	1.00	0.37	2	1	0.82	0.84	0.05	0.91	0.70
3	3	0.19	1.67	2.00	0.58	2	1	0.83	0.83	0.06	0.89	0.77
4	2	0.13	1.50	1.50	0.71	2	1	0.81	0.81	0.08	0.86	0.75
\$5	2	0.13	1.00	1.00	0.00	1	1	0.81	0.81	0.01	0.82	0.80
\$2	56	3.5	1.20	1.00	0.40	2	1	0.82	0.83	0.05	0.91	0.70

doi:10.1371/journal.pone.0104372.t001



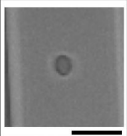
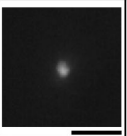

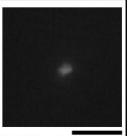
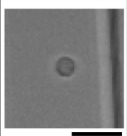
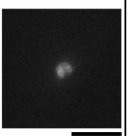
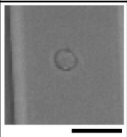
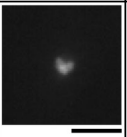
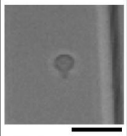
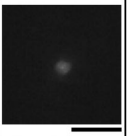
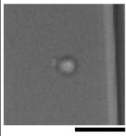
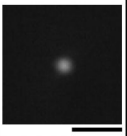
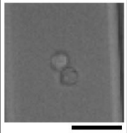
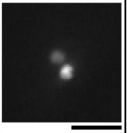

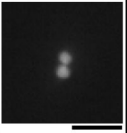
Cancer-implanted					Control				
Cluster size ( $N_n$ )	BF	FL	S [ $\mu\text{m}^2$ ]	$S_n$ [ $\mu\text{m}^2$ ]	Cluster size ( $N_n$ )	BF	FL	S [ $\mu\text{m}^2$ ]	$S_n$ [ $\mu\text{m}^2$ ]
1 (1) $n = 4005$			59	35	1 (1) $n = 1543$			55	21
1 (2) $n = 123$			57	41	1 (2)	N.A.			
1 (3) $n = 10$			72	47	1 (3)	N.A.			
2 (1) $n = 126$			67	26	2 (1) $n = 41$			69	40
2 (2) $n = 48$			117	74	2 (2) $n = 8$			73	61

Figure 7. Typical cell images for single and double cells in cancer cell-implanted and control blood. Each data count ( $n$ ) indicates the image number having the same cluster size and  $N_n$ . Bars, 20  $\mu\text{m}$ . doi:10.1371/journal.pone.0104372.g007

shape, which was expected for cell clusters. Figure 10 shows the relationship between the average value of  $R$  and cell cluster size for a cancer-implanted sample (detailed numbers are also shown in Table 1). As shown in the figure and table, all single cells had  $R$  higher than 0.90, with an average of 0.96, indicating that all cells having  $R$  smaller than 0.90 were clusters composed of more than 2 cells. On the other hand,  $R$  values for clusters composed of more than 2 cells were lower than 0.90 on average, and in detail, 131 clusters in cancer-implanted samples (55% of all clusters) and 55 clusters in control (98% of all clusters) had  $R$  lower than 0.90. Moreover, all large clusters composed of more than 3 cells having more than 3 nuclei, specifically observed only in cancer-implanted blood, had  $R$  lower than 0.90. These results indicate that more than half of the clusters, especially large clusters, could be identified by using  $R$  as an imaging biomarker.

According to the above results, large cluster formation of cancer cells in the blood was strongly expected. To confirm this, clusters larger than 300  $\mu\text{m}^2$  were collected by performing cell sorting in the chip, and their cell types were identified by measuring genome errors in the cells. Firstly, target genes that were included in the MAT-LyLu chromosome with abnormal copy numbers were searched by comparative genomic hybridization (CGH) assay using the cell line, with liver tissue of the rat as a reference. Two particularly abundant genes, *csp2* and *zdhc17* located on chromosome 7q13, were found (Fig. 11 (a)) and set as target genes for the identification of cancer cells in the blood. Next, the TaqMan copy number assay was performed for cells collected in

both the collection reservoir and the discarded reservoir (see Fig. 3). From the results, increases of copy numbers for both *csp2* and *zdhc17* were specifically observed for clustered cells collected in the collection reservoir (Fig. 11 (b)). These results indicate that large clusters, which were specifically observed in cancer cell-implanted blood, were CTCs.

### Discussion

In this study, four imaging biomarkers, cell area, nucleus area, number of nuclei, and perimeter ratio ( $S$ ,  $S_n$ ,  $N_n$ , and  $R$ ), were evaluated for the identification of cell clusters in the blood. From the results, some threshold values were obtained for each imaging biomarker, namely, (1)  $S$  larger than 200  $\mu\text{m}^2$  and (2)  $S_n$  larger than 90  $\mu\text{m}^2$  were specific to cancer cell-implanted blood. In addition, (3)  $N_n$  higher than 3 was also specific to cancer cell-implanted blood. Finally, (4) all clustered cells composed of more than 3 cells having  $N_n$  higher than 3, which was specific to cancer cell-implanted blood, had  $R$  lower than 0.90. According to these results, the use of  $R$  is one useful approach for the identification of clustered cells having multiple nuclei numbering more than 3, which are specific to cancer cell-implanted blood.  $S$  and  $S_n$  are also useful parameters for the identification of extremely large clusters, which are quite likely to be CTCs. For small clusters composed of two cells, it is in principle difficult to distinguish whether the cluster is an actual cluster or two independent cells flowing alongside each other by using image-based analysis. One potential approach to distinguish these possibilities is the

Cancer-implanted					Control				
Cluster size ( $N_n$ )	BF	FL	S [ $\mu\text{m}^2$ ]	$S_n$ [ $\mu\text{m}^2$ ]	Cluster size ( $N_n$ )	BF	FL	S [ $\mu\text{m}^2$ ]	$S_n$ [ $\mu\text{m}^2$ ]
3 (3) $n = 6$			251	126	3 (1) $n = 1$			53	12
4 (4) $n = 4$			258	147	4 (1) $n = 1$			197	20
6 (6) $n = 1$			388	179	5 (1) $n = 1$			99	32
15 (max., 10) $n = 1$			1163	342	6 (max., 1) $n = 1$			133	50

Figure 8. Typical cell images for clustered cells composed of more than three cells in cancer cell-implanted and control blood. Each data count ( $n$ ) indicates the image number having the same cluster size and  $N_n$ . Bars, 20  $\mu\text{m}$ .  
doi:10.1371/journal.pone.0104372.g008

combination of the image-based analysis suggested in this study with a molecular analytical approach, such as quantitative gene copy number assays of the targeted cells. The system developed in this study has been combined with a cell sorting unit and can perform the combination measurement of multi-imaging analysis with molecular analysis, as shown in Fig. 11, which indicates the advantage of our developed system.

For the detection of CTCs, some methods were suggested. The principles were in general separated into two kinds; one was based on the chemical reaction and the other was physical detection. The former is in general based on the labeling of target molecules on the CTCs with antibodies, and it was sometimes combined with microfabrication technologies to improve detection sensitivities [6,7]. However, this approach sometimes yielded false-negative detection because of the variety of molecular expression levels in

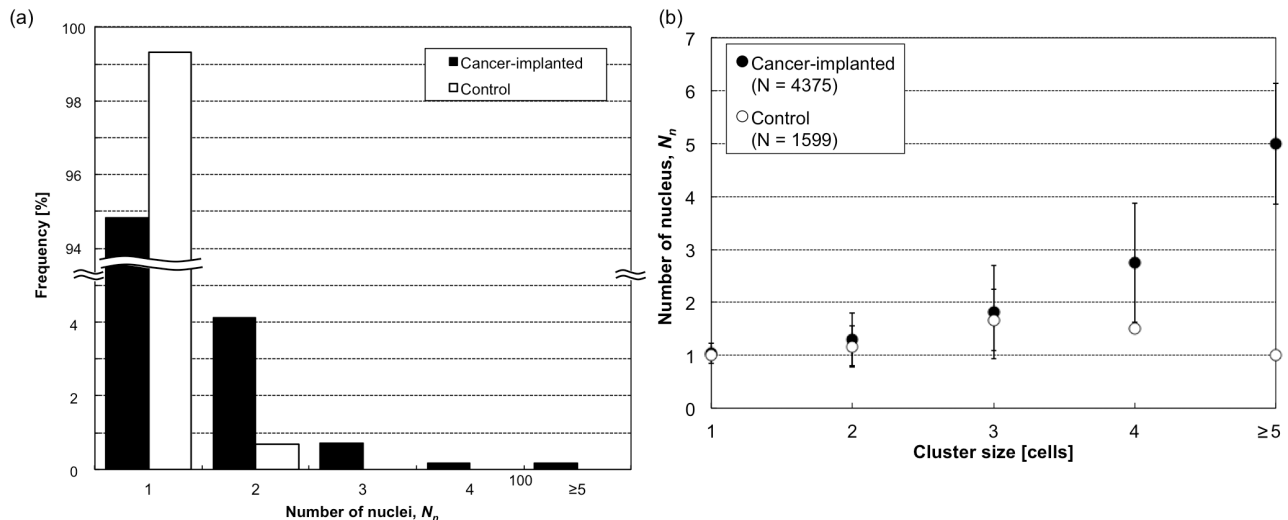


Figure 9. Summary of the number of nuclei,  $N_n$ . (a) A histogram of  $N_n$  obtained from cancer cell-implanted and control blood. (b) The relationship between  $N_n$  and cell cluster size.  
doi:10.1371/journal.pone.0104372.g009

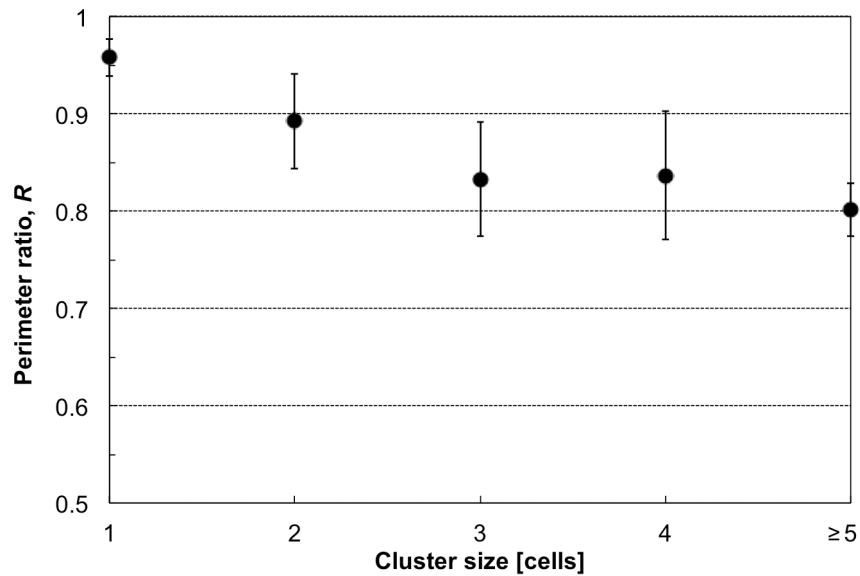


Figure 10. The relationship between perimeter ratio, R, and cell cluster size obtained from cancer cell-implanted blood. doi:10.1371/journal.pone.0104372.g010

CTCs. For this latter case, various physical parameters of CTCs such as cell diameter [4,16,17] and dielectrophoretic properties [5] have been used with a combination of microfabrication technologies. According to the results in this study, cell size (S) is one useful parameter to find irregular cells in blood samples such as

clustered cells; however, the use of only one parameter is insufficient for the exhaustive detection of CTCs. Our developed system can use various parameters including both chemical and physical properties to find target cells, which would also be useful for the detection of various CTCs.

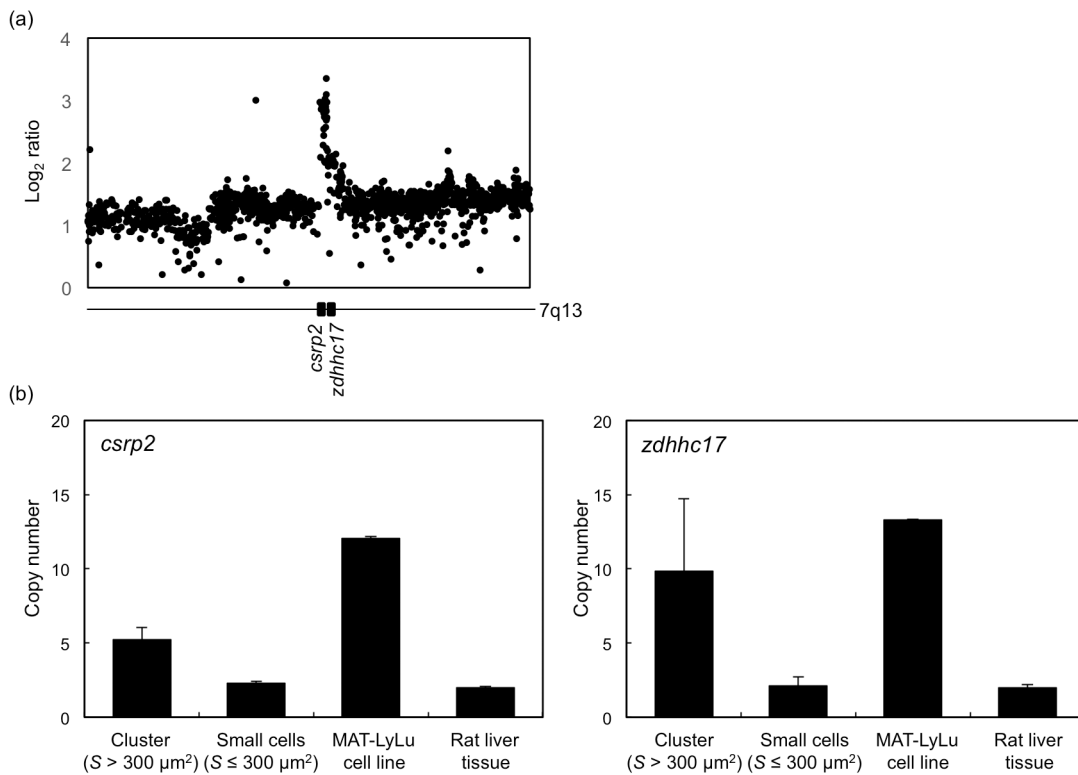


Figure 11. Results of quantitative gene copy number assays. (a) Results of CGH assays performed for the MAT-LyLu cell line. Liver tissue of the rat was used as a reference. Gene amplifications for *csrp2* and *zdhhc17* located on chromosome 7q13 were found. (b) Results of TaqMan copy number assays performed with clusters larger than  $300 \mu m^2$  collected in the collection reservoir, and cells smaller than  $300 \mu m^2$  collected in the discarded reservoir. Results of the assays for the MAT-LyLu cell line (positive control) and liver tissue (negative control) are also shown. doi:10.1371/journal.pone.0104372.g011

In this study, large clusters were specifically observed in cancer cell-implanted blood, and an approach for finding these clusters in the blood has possibility for the development of a new cancer metastasis diagnostic method. Results in this study were obtained using hemolyzed blood samples *in vitro*; therefore, the large cluster formations should also be confirmed for blood *in vivo* as a next step to achieve such a new diagnostic method. One possibility for the mechanism of large cluster formation is an aggregation of implanted cancer cells by immune reaction of the rat with antibody formation. In this study, blood samples were picked up from the rat 2 weeks after implantation; therefore, time-course measurements of cluster formations after implantation might be one useful way to confirm the above possibility, and our developed system can also be used to confirm this.

## Conclusion

In this study, an on-chip multi-imaging flow cytometry system was developed to find cell clusters in blood samples. The system can take both BF and FL pictures simultaneously, and can obtain imaging biomarkers; cell area, nucleus area, number of nuclei, and perimeter ratio ( $S$ ,  $S_n$ ,  $N_n$ , and  $R$ ), in real time. By using the developed system, sample blood of rats in which cancer cells had been pre-implanted was measured and compared with that of

healthy rats. In terms of the results, clustered cells having (1)  $S$  larger than  $200 \mu\text{m}^2$  and (2)  $S_n$  larger than  $90 \mu\text{m}^2$  were specifically observed in cancer cell-implanted blood, but were not observed in healthy rats. In addition, (3)  $N_n$  higher than 3 was specific for cancer-implanted blood and (4)  $R$  smaller than 0.90 was specific for all clusters having  $N_n$  higher than 3, which were specific for cancer-implanted blood. Finally, quantitative gene copy number assay was performed for the large clusters, and they were shown to be CTCs. These results indicate the usefulness of the imaging biomarkers for characterizing clusters, and that the developed system is useful to identify clustered CTCs in blood.

## Acknowledgments

We gratefully thank Mr. S. Kawada and Ms. H. Mikami for technical assistance.

## Author Contributions

Conceived and designed the experiments: HK TA KN YM KY. Performed the experiments: HK HT YN KS AH MO MG TA. Analyzed the data: HK KS AH MO MG TA KN YM KY. Contributed reagents/materials/analysis tools: HK HT YN KS AH MO MG TA KN YM KY. Wrote the paper: HK KY.

## References

- Cristofanilli M, Budd GT, Ellis MJ, Stopeck A, Matera J, et al. (2004) Circulating tumor cells, disease progression, and survival in metastatic breast cancer. *N Engl J Med* 351: 781–791.
- Sethi N, Kang Y (2011) Unravelling the complexity of metastasis - molecular understanding and targeted therapies. *Nat Rev Cancer* 11: 735–748.
- Yu M, Stott S, Toner M, Maheswaran S, Haber DA (2011) Circulating tumor cells: approaches to isolation and characterization. *J Cell Biol* 192: 373–382.
- Davis JA, Inglis DW, Morton KJ, Lawrence DA, Huang LR, et al. (2006) Deterministic hydrodynamics: taking blood apart. *Proc Natl Acad Sci U S A* 103: 14779–14784.
- Gascoyne PR, Noshari J, Anderson TJ, Becker FF (2009) Isolation of rare cells from cell mixtures by dielectrophoresis. *Electrophoresis* 30: 1388–1398.
- Nagrath S, Sequist LV, Maheswaran S, Bell DW, Irimia D, et al. (2007) Isolation of rare circulating tumour cells in cancer patients by microchip technology. *Nature* 450: 1235–1239.
- Stott SL, Hsu CH, Tsukrov DI, Yu M, Miyamoto DT, et al. (2010) Isolation of circulating tumor cells using a microvortex-generating herringbone-chip. *Proc Natl Acad Sci U S A* 107: 18392–18397.
- Zheng S, Lin HK, Lu B, Williams A, Datar R, et al. (2011) 3D microfilter device for viable circulating tumor cell (CTC) enrichment from blood. *Biomed Microdevices* 13: 203–213.
- Budd GT, Cristofanilli M, Ellis MJ, Stopeck A, Borden E, et al. (2006) Circulating tumor cells versus imaging—predicting overall survival in metastatic breast cancer. *Clin Cancer Res* 12: 6403–6409.
- Danila DC, Heller G, Gignac GA, Gonzalez-Espinoza R, Anand A, et al. (2007) Circulating tumor cell number and prognosis in progressive castration-resistant prostate cancer. *Clin Cancer Res* 13: 7053–7058.
- Takahashi K, Hattori A, Suzuki I, Ichiki T, Yasuda K (2004) Non-destructive on-chip cell sorting system with real-time microscopic image processing. *J Nanobiotechnology* 2: 5.
- Hayashi M, Hattori A, Kim H, Terazono H, Kaneko T, et al. (2011) Fully automated on-chip imaging flow cytometry system with disposable contamination-free plastic re-cultivation chip. *Int J Mol Sci* 12: 3618–3634.
- Yasuda K, Hattori A, Kim H, Terazono H, Hayashi M, et al. (2013) Non-destructive on-chip imaging flow cell-sorting system for on-chip cellomics. *Microfluidics and Nanofluidics* 14: 907–931.
- Vona G, Sabile A, Louha M, Sitruk V, Romana S, et al. (2000) Isolation by size of epithelial tumor cells - A new method for the immunomorphological and molecular characterization of circulating tumor cells. *American Journal of Pathology* 156: 57–63.
- Desitter I, Guerrouahen BS, Benali-Furet N, Wechsler J, Janne PA, et al. (2011) A New Device for Rapid Isolation by Size and Characterization of Rare Circulating Tumor Cells. *Anticancer Research* 31: 427–441.
- Hosokawa M, Kenmotsu H, Koh Y, Yoshino T, Yoshikawa T, et al. (2013) Size-Based Isolation of Circulating Tumor Cells in Lung Cancer Patients Using a Microcavity Array System. *Plos One* 8.
- Hosokawa M, Yoshikawa T, Negishi R, Yoshino T, Koh Y, et al. (2013) Microcavity Array System for Size-Based Enrichment of Circulating Tumor Cells from the Blood of Patients with Small-Cell Lung Cancer. *Analytical Chemistry* 85: 5692–5698.
- Abdalla F, Boder J, Markus R, Hashmi H, Buhmeida A, et al. (2009) Correlation of nuclear morphometry of breast cancer in histological sections with clinicopathological features and prognosis. *Anticancer Res* 29: 1771–1776.
- Buhmeida A, Algars A, Ristamaki R, Collan Y, Syrjanen K, et al. (2006) Nuclear size as prognostic determinant in stage II and stage III colorectal adenocarcinoma. *Anticancer Res* 26: 455–462.
- de Andrea CE, Petrilli AS, Jesus-Garcia R, Bleggi-Torres LF, Alves MT (2011) Large and round tumor nuclei in osteosarcoma: good clinical outcome. *Int J Clin Exp Pathol* 4: 169–174.
- Deans GT, Hamilton PW, Watt PC, Heatley M, Williamson K, et al. (1993) Morphometric analysis of colorectal cancer. *Dis Colon Rectum* 36: 450–456.
- Dundas SA, Laing RW, O’Cathain A, Seddon I, Slater DN, et al. (1988) Feasibility of new prognostic classification for rectal cancer. *J Clin Pathol* 41: 1273–1276.
- Meachem MD, Burgess HJ, Davies JL, Kidney BA (2012) Utility of nuclear morphometry in the cytologic evaluation of canine cutaneous soft tissue sarcomas. *J Vet Diagn Invest* 24: 525–530.
- Sokmen S, Sarioglu S, Fuzun M, Terzi C, Kupelioglu A, et al. (2001) Prognostic significance of angiogenesis in rectal cancer: a morphometric investigation. *Anticancer Res* 21: 4341–4348.
- Tennant TR, Kim H, Sokoloff M, Rinker-Schaeffer CW (2000) The Dunning model. *Prostate* 43: 295–302.
- Hattori A, Yasuda K (2010) Comprehensive Study of Microgel Electrode for On-Chip Electrophoretic Cell Sorting. *Japanese Journal of Applied Physics* 49: 06GM04.
- Hattori A, Kim H, Terazono H, Odaka M, M G, et al. (2014) Identification of cells using morphological information of bright field/fluorescent multi-imaging flow cytometer images. *Japanese Journal of Applied Physics*, in press.
- Kinosita K, Jr., Itoh H, Ishiwata S, Hirano K, Nishizaka T, et al. (1991) Dual-view microscopy with a single camera: real-time imaging of molecular orientations and calcium. *J Cell Biol* 115: 67–73.
- Nomura F, Kaneko T, Hattori A, Yasuda K (2011) Label-Free Shape-Based Selection of Cardiomyocytes with on-Chip Imaging Cell Sorting System. *J Bioprocess Biotechniq* S3:003.



## Analytical performance of the cobas EGFR mutation assay for Japanese non-small-cell lung cancer



Hideharu Kimura<sup>a</sup>, Tatsuo Ohira<sup>b</sup>, Osamu Uchida<sup>c</sup>, Jun Matsubayashi<sup>d</sup>,  
Shinichiro Shimizu<sup>e</sup>, Toshitaka Nagao<sup>d</sup>, Norihiko Ikeda<sup>b</sup>, Kazuto Nishio<sup>a,\*</sup>

<sup>a</sup> Department of Genome Biology, Kinki University Faculty of Medicine, 337-2 Ohno-Higashi, Osaka-Sayama, Osaka 589-8511 Japan

<sup>b</sup> Department of Surgery, Tokyo Medical University, 6-7-1 Nishi-shinjuku, Shinjuku-ku, Tokyo 160-0023, Japan

<sup>c</sup> Department of Respiratory Surgery, Funabashi Municipal Medical Center, 1-21-1 Kanasugi, Funabashi, Chiba 273-8588, Japan

<sup>d</sup> Department of Anatomic Pathology, Tokyo Medical University, 6-7-1 Nishi-shinjuku, Shinjuku-ku, Tokyo 160-0023, Japan

<sup>e</sup> Department of Pathology, Funabashi Municipal Medical Center, 1-21-1 Kanasugi, Funabashi, Chiba 273-8588, Japan

### article info

#### Article history:

Received 27 October 2013

Received in revised form

11 December 2013

Accepted 20 December 2013

#### Keywords:

Non-small-cell lung cancer

EGFR mutation

EGFR-TKI treatment

cobas<sup>®</sup> EGFR Mutation Test

Companion diagnostics

Personalised healthcare

### abstract

**Introduction:** Clinical outcomes in non-small-cell lung cancer (NSCLC) patients with epidermal growth factor receptor (EGFR) mutations have been reported to be correlated with the use of EGFR-tyrosine kinase inhibitors (EGFR-TKIs). Therefore, it is essential to confirm the presence of EGFR mutations using highly sensitive testing methods. In this study, we compared the performance of the cobas<sup>®</sup> EGFR Mutation Test (cobas EGFR assay) and the theascreen<sup>®</sup> EGFR RGQ PCR Kit (therascreen EGFR assay) for use as an in vitro diagnostic (IVD) product.

**Methods:** We extracted DNA from 150 formalin-fixed, paraffin-embedded tissue samples from 150 patients diagnosed with NSCLC, and performed a comparative study of the cobas EGFR and theascreen EGFR assay methods. All discordant results were re-analyzed by direct sequencing.

**Results:** The concordance rate between the cobas EGFR assay and the theascreen EGFR assay was 98.0% (145/148). EGFR mutations were detected at a frequency of 40.9% (61/149) in NSCLC specimens using the cobas EGFR assay and 40.2% (60/149) using the theascreen EGFR assay. Three discrepant results were found in this study. Two double mutations were detected by the cobas EGFR assay but only one in the theascreen EGFR assay. No invalid results resulted from sample analysis by the cobas EGFR assay.

**Conclusions:** Our results show a high concordance rate (98.0%) of cobas EGFR assay with an existing IVD product, the theascreen EGFR assay. Since they are IVD diagnostic products, both assays proved to be simple, validated methods in detecting the most common, clinically significant EGFR mutations and proved to be helpful for appropriate treatment guidance for NSCLC patients.

© 2014 Elsevier Ireland Ltd. All rights reserved.

### 1. Introduction

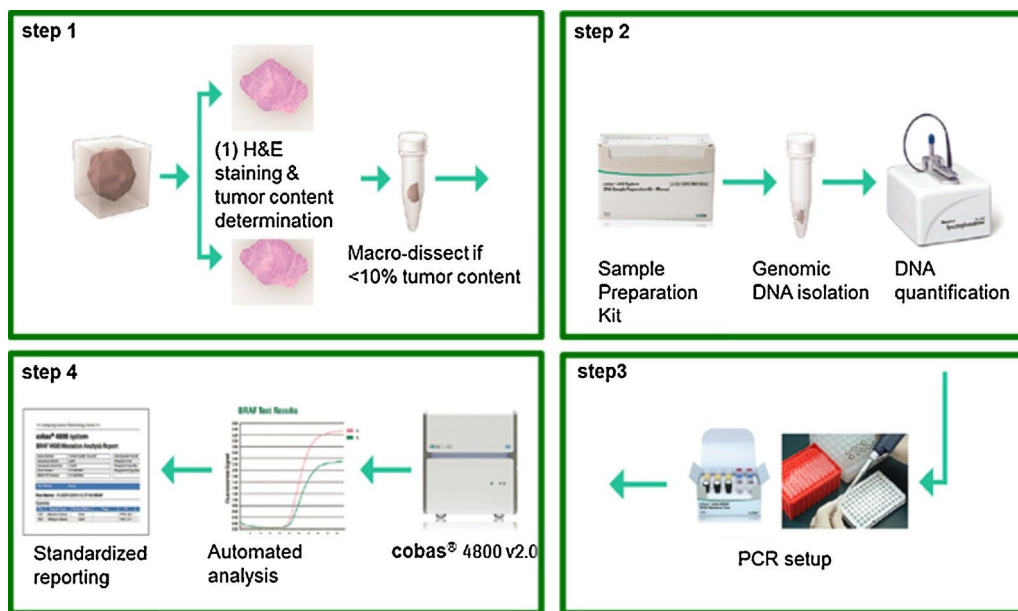
Non-small-cell lung cancer (NSCLC) patients frequently have activating EGFR mutations and respond well to treatment with small molecule EGFR-tyrosine kinase inhibitors (TKIs) such as gefitinib and erlotinib [1–4]. Both the American Society of Clinical Oncology and the Japan Lung Cancer Society recommend EGFR mutation testing in patients being considered for EGFR-TKI treatment as a first-line therapy [5]. Similar guidelines recommending testing for EGFR mutations were established by the College of American Pathologists, the International Association for the Study of Lung Cancer, and the Association for Molecular Pathology [6]. Patients' EGFR mutation status prior to the commencement of treatment impacts outcomes and, as a result, EGFR testing has been

developed as a companion diagnostic; this relationship between therapeutic and diagnostic agents contributes to personalized healthcare. Recently, it was reported that about half of patients who are initially sensitive to EGFR-TKIs may acquire resistance to EGFR-TKIs [7] following a period of therapy, mainly as a result of the appearance of EGFR mutations associated with resistance to treatment, such as T790M. Indeed, a recent study suggested that the T790M mutation may be present in a small proportion of tumor cells prior to treatment, with the proportion of mutant alleles increasing gradually during treatment [8]. Similar findings were observed for exon 20 insertions; that they are usually associated with primary or de novo resistance to EGFR-TKI therapy [9]. Thus, it is important to re-assess EGFR mutation status during treatment to determine the most appropriate treatment regimens for patients.

A number of PCR-based techniques are used in the clinic for the assessment of EGFR mutations. In Japan, the “Scorpion-ARMS” theascreen<sup>®</sup> EGFR Rotor-Gene Q (RGQ) PCR Kit (therascreen EGFR

\* Corresponding author. Tel.: +81 72 366 0221; fax: +81 072 367 6369.

E-mail address: [knishio@med.kindai.ac.jp](mailto:knishio@med.kindai.ac.jp) (K. Nishio).



**Fig. 1.** Assay flow for the cobas EGFR mutation assay. The assay is composed of four steps. Step 1: 5- $\mu$ m sections are prepared from FFPE tissue. One section is used for H&E staining to assess tumor content and the other section is used for DNA isolation. Step 2: Genomic DNA is isolated using the cobas<sup>®</sup> DNA Sample Preparation Kit. Step 3: DNA is mixed with reagents after quantification. Step 4: DNA is amplified using the cobas z 480 system. Results are automatically reported.

assay; Qiagen, Hilden, Germany) is the only available in vitro diagnostic (IVD) test.

In this study, we compared the performance of the cobas EGFR assay and the theascreen EGFR assay using formalin-fixed, paraffin-embedded (FFPE) tissue specimens from NSCLC patients.

## 2. Materials and methods

### 2.1. Tissue samples

A series of archived 150 FFPE tissue samples which was surgically resected from 150 Japanese patients diagnosed with NSCLC, collected between March 2011 and December 2012, was obtained from Tokyo Medical University (Tokyo, Japan) and Funabashi Medical Hospital (Funabashi, Japan). All patients enrolled in the study provided informed consent for the use of resected tissue. The study was approved by the ethics committee of each participating institute and conducted according to Institutional Review Board guidelines.

### 2.2. cobas EGFR Mutation Test

The cobas EGFR assay is an allele-specific real-time PCR system (Figure, Supplemental Digital Content 1; Fig. 1) that qualitatively measures the amplification of DNA to identify 41 mutations in exons 18–21 of the EGFR gene from 50 ng of DNA derived from human FFPE NSCLC tissues (Table, Supplemental Digital Content 2). Within each reaction mixture, exon 28 was amplified as an internal control. DNA isolation, amplification/detection, and result reporting can be performed in less than 8 h with up to 30 specimens processed simultaneously. The cobas EGFR assay has fully automated results reporting.

### 2.3. Specimen preparation for cobas EGFR assay

Two FFPE tissue sections of 5  $\mu$ m thickness were prepared for this assay. One was used for DNA extraction and the other was used to confirm the presence of tumor content by hematoxylin and eosin

(H&E) staining, which was performed by a pathologist. Any specimen containing <10% tumor content by area was macrodissected.

### 2.4. DNA extraction

FFPE tissue specimens were deparaffinized and then DNA extraction was performed according to the standard procedure described in the cobas<sup>®</sup> DNA Sample Preparation Kit (Roche Molecular Systems, Inc., USA) package insert. Briefly, the sample was incubated for 1 h at 56 °C and then for additional one hour at 90 °C in the presence of a protease and chaotropic lysis/binding buffer that causes the release of nucleic acids but protects released genomic DNA from degradation by DNase. The amount of genomic DNA was spectrophotometrically determined and adjusted to a fixed concentration of 2 ng/ $\mu$ L.

### 2.5. PCR amplification and detection

A total of 150 ng of DNA is required for the cobas EGFR assay. Target DNA was amplified and detected using the cobas<sup>®</sup> z480 analyzer (Roche Molecular Systems Inc.) according to the instructions for the cobas<sup>®</sup> EGFR Mutation Test, which measures the fluorescence generated by specific PCR products. All results were automatically performed by cobas<sup>®</sup> 4800 software.

### 2.6. theascreen<sup>®</sup> EGFR RGQ PCR Kit

The theascreen assay is a real time-PCR assay that combines the Amplification Refractory Mutation System (ARMS) and Scorpions fluorescent primer/probe system. It can detect 29 somatic mutations in exons 18–21 of EGFR. A maximum of 7 results can be obtained from one run. The theascreen EGFR assay was performed according to the manufacturer's guidelines (Qiagen). Briefly, DNA was isolated from FFPE tissue samples and the total sample DNA assessed by amplifying a region of exon 2 from EGFR by PCR. Next, the DNA samples were tested for the presence or absence of EGFR mutations by real-time PCR using a Scorpion probe and primers specific for wild type and mutant EGFR DNA. The difference

**Table 1**  
Clinical characteristics of the patients providing surgically resected FFPE samples in NSCLC.

	N = 149
Gender	
Male	75
Female	74
Age	
Younger than 65 years	42
Older than 65 years	107
Histology	
Adenocarcinoma or adeno-squamous cell carcinoma (Ad)	126
Squamous cell carcinoma (Sq)	17
Large cell carcinoma (Ia)	2
Other	4
Smoking history	
Smoker	18
Ever smoker	73
Never smoker	56
ND	2

ND, not determined; N, number.

between the mutation assay cycle threshold ( $C_T$ ) and control assay  $C_T$  from the same sample was used to calculate sample  $\Delta C_T$  values. Samples designated mutation positive if the  $\Delta C_T$  was less than the cutoff  $\Delta C_T$  value.

### 2.7. Sanger sequencing

DNA samples obtained from specimens that were discordant between cobas EGFR and therascreen EGFR assays were amplified using the following site-specific primers: Exon 18 Forward, 5'-TGGAGCCTTACACCCAGT-3', Reverse, 5'-ACAGCTTGCAAGGACTCTGG-3'; Exon 19 Forward, 5'-TCTGGATCCCAGAAGGTGAG-3', Reverse, 5'-CAGCTGCCAGACATGAGAAA-3'; Exon 20 Forward, 5'-CATTTCATGCGTCTTCACCTG-3', Reverse, 5'-GTCTTTGTGTTCCCGGACAT-3'; Exon 21 Forward, 5'-GATCTGTCCCTCAGCAGGGTC-3', Reverse, 5'-GGCTGACCTAAAGCCACCTCC-3'. The fragments were subcloned into the Zero Blunt TOPO vector (Zero Blunt TOPO PCR Cloning Kit; Life Technologies, USA). Direct sequencing was performed with 100 colonies from one specimen by ABI3100 Genetic Analyzer (ABI) using the BigDye<sup>®</sup> Terminators v3.1 Cycle Sequencing Kit (Life Technologies). One mutation detected in 100 results was classed as "Mutation Detected" in this study. This assay required 1  $\mu$ g of genomic DNA from specimens. Sanger sequencing was performed with the specimen that resulted double mutation (L858R and M790M) from cobas EGFR assay but single mutation (L858R) from therascreen EGFR assay at Mitsubishi Chemical Medicine Corporation followed by daily routine. The sequencing result was used as Golden standard.

## 3. Results

### 3.1. Study population

A series of 150 FFPE tissue samples from patients diagnosed with NSCLC was examined. One specimen was excluded owing to a lack of a completed consent form, leaving 149 samples available for analysis. The clinical and pathological characteristics of the patients providing the evaluable specimens are summarized in Table 1.

### 3.2. EGFR mutation types

EGFR mutations were identified in 63 NSCLC specimens (42.3%) using the cobas EGFR assay and 61 specimens (40.9%) using the

**Table 2**  
Methods correlation between mutation findings using the cobas EGFR and therascreen EGFR assays.

		therascreen			Total
		MD	MND	Invalid	
cobas	MD	59	2	0	61
	MND	1	86	1	88
	Invalid	0	0	0	0
	Total	60	88	1	149

MD, mutation detected; MND, mutation not detected.

**Table 3**  
Detailed concordant rate between cobas EGFR and therascreen EGFR assays.

Mutation	MD concordance	MND concordance	Total concordance
G719X	100% (3/3)	100% (145/145)	100% (148/148)
exon19del	95.7% (22/23)	100% (125/125)	99.3% (146/147)
S768I	100% (1/1)	99.3% (146/147)	99.3% (147/148)
T790M	–	99.3% (147/148)	99.3% (147/148)
exon20ins	–	100% (148/148)	100% (148/148)
L858R	100% (34/34)	99.1% (113/114)	99.3% (147/148)

Del, deletion; Ins, insertion; MD, mutation detected; MND, mutation not detected.

therascreen EGFR assay (Table, Supplementary Digital Content 4). Exon 19 deletions (Ex19del) and a point mutation (L858R) accounted for 90.5% (57/63) and 93.4% (57/61) of all mutations identified using the cobas EGFR assay and therascreen EGFR assay, respectively (Table, Supplementary Digital Content 3). This confirms the findings of a previous study [10], which found that Ex19del and L858R mutations accounted for 90% of NSCLC EGFR activating mutations. The exon 20 insert mutation (Ex20Ins) was not observed in any of the samples tested in this study. A T790M point mutation was detected by the cobas EGFR assay (0.68%) but not by the therascreen EGFR assay.

### 3.3. Invalid test rate

Mutation analysis of exons 18–21 of the EGFR gene was successfully performed in all 149 specimens (100%) using the cobas EGFR assay. In contrast, in experiments using the therascreen EGFR assay, two test specimens initially gave invalid test results. In those cases, DNA was extracted from new FFPE tissue samples. However, because one sample gave an invalid result again, this case was excluded from the analysis, resulting in an invalid rate of 0.68% (1/148) for the therascreen EGFR assay (Table 2). In addition, one invalid control occurred in the therascreen EGFR assay (data not shown).

### 3.4. Method correlation agreement analysis

The correlation rate between cobas EGFR assay and therascreen EGFR assay was 98.0%. Of the 149 evaluable samples tested, only three discordants between the two EGFR mutation assays were observed (Table 3).

### 3.5. Re-analysis of discordants by direct sequencing

Test specimens that gave discordant results between the cobas EGFR and therascreen EGFR assays were retested using direct sequencing from sub-cloned samples (Table 4). A discordant MND by therascreen EGFR assay was observed by direct sequencing to be an L858R point mutation, confirming the MD result assessed by cobas EGFR assay. In addition, an Ex19del mutation identified as MD by therascreen EGFR assay was shown to be MND by direct sequencing, again confirming the cobas EGFR assay result. The cobas EGFR assay identified one case with a double mutation, L858R and T790M

**Table 4**  
Re-analysis of discordants by direct sequencing.

	therascreen		Cobas		Sequencing (reanalysis)
Sample 1	MND	–	MD	L858R	MD
Sample 2	MD	EX19Del	MND	–	MND
Sample 3	MND	–	MD	S768I	MND
Sample 4	MD	L858R	MD	L858R,T790M	L858R

Del, deletion; Ins, insertion; MD, mutation detected; MND, mutation not detected.

**Table 5**  
Re-analysis: combined therascreen EGFR assay and Sanger sequencing for resolution of discordant results.

		therascreen and/or Sanger sequencing	
		MD	MND
cobas	MD	60	1
	MND	0	87

MD, mutation detected; MND, mutation not detected.

(Table 4). However, only the L858R mutation was identified by the therascreen EGFR assay and only the T790M mutation was detected by direct sequencing. We then performed a re-analysis using a combination of the therascreen EGFR assay and Sanger sequencing for resolution of the discordant results (Table 5). This demonstrated an MD concordance rate of 100% (60/60), an MND concordance rate of 98.9% (87/88) and a total concordance rate of 99.3% (147/148) between the tests.

#### 4. Discussion

The overall correlation results of the cobas EGFR assay, an existing EGFR mutation screening method (the therascreen EGFR assay) plus direct sequencing was 99.3% (147/148) (Table 5). It also indicated that the cobas assay is at least as robust method to detect the most common clinically significant EGFR mutations as the existing therascreen EGFR assay.

Although we identified 3 discordant results among 149 (2.0%) specimens in this study, retesting by direct sanger sequencing confirmed that two of the three discordant results were in fact correctly called by the cobas EGFR assay. Although both assays share similar characteristics in terms of amplification methods and detection principles, the slight differences (e.g. probe and primer construction) between the two of them, influenced their sensitivities to the mutations. Also, the remaining discordant result analysis highlighted the importance of the purity of the extracted DNA for the PCR amplification. In fact, an Ex 20 S768I mutation identified as Mutation Detected (MD) by the cobas EGFR assay but not the therascreen EGFR assay, was not detected by direct sequencing, either. In this case, direct sequencing failed more than two times to detect the EGFR gene when using the extracted DNA from the QIAmp DNA FFPE Tissue extraction kit (Qiagen) suggesting that the quality of the DNA was not adequate for the testing (data not shown). This potential difference in DNA quality might be the reason why we have experienced discordant results in some cases.

One T790M mutation was detected together with L858R by the cobas EGFR assay in this study. As there is known heterogeneity with regard to the T790M mutation within tumor cells, it is difficult to mention that the extracted DNA was completely the same, even if we used serial sections. However the raw data from the cobas system showed high enough signals to robustly detect the mutation (data not shown). According to the package insert, cobas EGFR needs at least 3.13 ng DNA which includes 5% mutated DNA to detect the mutation. Therefore it appears that the cobas test might

be more sensitive than the therascreen test because, according to the therascreen package insert, it needs 7.02% mutated DNA within the input DNA [11,12].

About half of the patients who are initially sensitive to EGFR-TKIs may acquire resistance to EGFR-TKIs [7] following a period of therapy, mainly because of the selection for the cells with the T790M mutation in EGFR. In addition, the correlation between the presence of intrinsic T790M mutations and patient outcomes has been shown [8], and is probably related to the slow growth of tumors bearing the T790M mutation. Thus, it is important to re-assess EGFR mutation status during treatment in order to determine the most appropriate treatment regimens for patients.

For IVD products, it is important to have rapid and simple testing. The cobas EGFR assay has two advantages over the therascreen assay in this regard. One is that the process consists of easily performed and stable methods. Additionally, it takes only 8 h to go from tumor specimen to results using the semi-automated system. Thus, patients assessed using the cobas EGFR assay can begin the most appropriate treatment within a shorter time period. The other advantage is that only a very small amount of DNA (150 ng) is required to detect the tumor mutation status using the cobas EGFR assay. Moreover, it confirms the accuracy of the results by co-amplification of an internal control (i.e. exon 28). One of the issues associated with detecting EGFR mutations in advanced NSCLC patients is not obtaining a sufficient quantity of specimen to confirm the presence/absence of several biomarkers. It is important to be able to perform tests using just a small amount of DNA; thus, the cobas EGFR assay is suitable and reliable for the detection of targeted common EGFR mutations. In this study, we had high concordance with surgically resected specimens which had enough tumors. However, at clinical practice, minimal invisible samples such as pleural effusion or bronchial wash would be used from advanced NSCLC patients having difficulty of collecting tissue. To access this difficulty, even if the samples are small enough, at least confirming the amount of tumor cells by pathologist is required to have appropriate test result. Under the condition, it might be able to provide reliable result even if using either FFPE samples or cytology samples. It is important to accumulate the data with cytology samples which makes improvement of suitable testing for advanced NSCLC patients in the future.

#### 5. Conclusion

In the near future, more mutations that can serve as predictive markers for molecular-targeted treatments will be discovered, and mutation detection tests will play an increasingly important role in the clinical setting. The benefits of treatment will be maximized only if used together with clinically validated and accurate companion diagnostics. The cobas system offers the possibility of detecting additional mutations, not only mutations of EGFR. The combination of the cobas system with molecular-targeted treatments represents an important tool for physicians, supporting their efforts to effectively treat tumors.

#### Conflict of interest

Hideharu Kimura, Tatsuo Ohira, Osamu Uchida, Jun Matsubayashi, Shinichirou Shimizu, Toshitaka Nagao, Kazuto Nishio, Norihiko Ikeda was funded by Roche Diagnostics K.K. (Tokyo, Japan). There was no other financial support for the investigators.

#### Acknowledgements

This study was sponsored by Roche Diagnostics K.K. This means that the publication of this study is written by investigators and has no relative value of the cobas EGFR test for the promotion.



## Appendix A. Supplementary data

Supplementary data associated with this article can be found, in the online version, at <http://dx.doi.org/10.1016/j.lungcan.2013.12.012>.

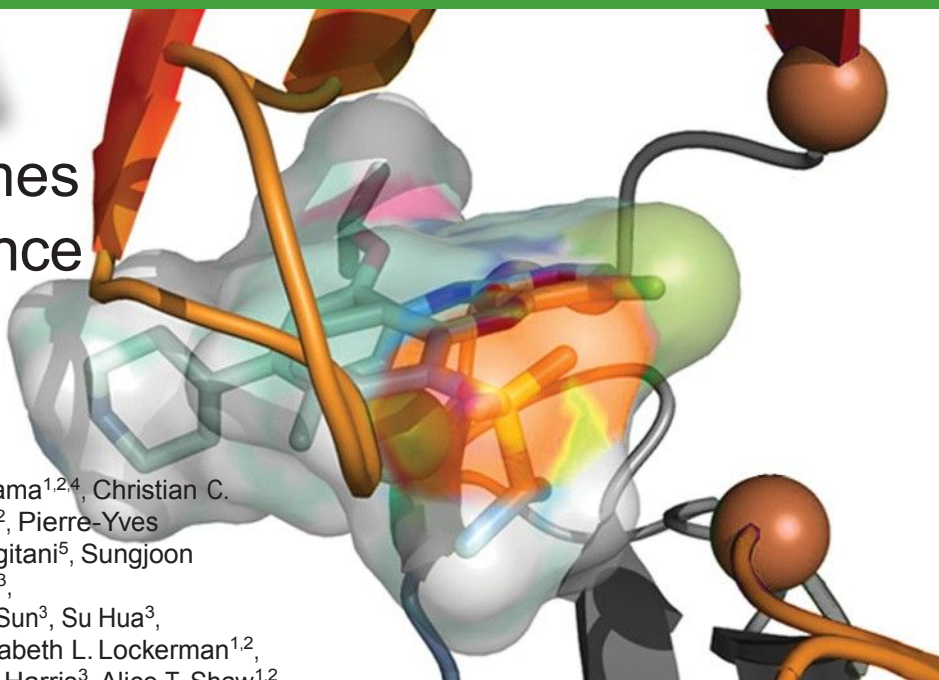
## References

- [1] Zhou C, Wu YL, Chen G, Feng J, Liu XQ, Wang C, et al. Erlotinib versus chemotherapy as first-line treatment for patients with advanced EGFR mutation-positive non-small-cell lung cancer (OPTIMAL, CTONG-0802): a multicentre, open-label, randomised, phase 3 study. *Lancet Oncol* 2011;12: 735–42.
- [2] Mok TS, Wu YL, Thongprasert S, Yang CH, Chu DT, Saijo N, et al. Gefitinib or carboplatin-paclitaxel in pulmonary adenocarcinoma. *N Engl J Med* 2009;361:947–57.
- [3] Rosell R, Carcereny E, Gervais R, Vergnenegre A, Massuti B, Felip E, et al. Erlotinib versus standard chemotherapy as first-line treatment for European patients with advanced EGFR mutation-positive non-small-cell lung cancer (EORTAC): a multicentre, open-label, randomized phase 3 trial. *Lancet Oncol* 2012;13:239–46.
- [4] Maemondo M, Inoue A, Kobayashi K, Sugawara S, Oizumi S, Isobe H, et al. Gefitinib or chemotherapy for non-small-cell lung cancer with mutated EGFR. *N Engl J Med* 2010;362:2380–8.
- [5] Keedy VL, Temin S, Somerfield MR, Beasley MB, Johnson DH, McShane LM, et al. American Society of Clinical Oncology provisional clinical opinion: epidermal growth factor receptor (EGFR) mutation testing for patients with advanced non-small-cell lung cancer considering first-line EGFR tyrosine kinase inhibitor therapy. *J Clin Oncol* 2011;29: 2121–7.
- [6] Lindeman NI, Cagle PT, Beasley MB, Chitale DA, Dacic S, Giaccone G, et al. Molecular testing guideline for selection of lung cancer patients for EGFR and ALK tyrosine kinase inhibitors: guideline from the College of American Pathologists, International Association for the Study of Lung Cancer, and Association for Molecular Pathology. *J Thorac Oncol* 2013;(April) [Epub ahead of print].
- [7] Nguyen KS, Kobayashi S, Costa DB. Acquired resistance to epidermal growth factor receptor tyrosine kinase inhibitors in non-small-cell lung cancers dependent on the epidermal growth factor receptor pathway. *Clin Lung Cancer* 2009;10:281–9.
- [8] Fujita Y, Suda K, Kimura H, Matsumoto K, Arai T, Nagai T, et al. Highly sensitive detection of EGFR T790M mutation using colony hybridization predicts favorable prognosis of patients with lung cancer harboring activating EGFR mutation. *J Thorac Oncol* 2012;7:1640–4.
- [9] Yasuda H, Kobayashi S, Costa DB. EGFR exon 20 insertion mutations in non-small-cell lung cancer: preclinical data and clinical implications. *Lancet Oncol* 2012;13:e23–31.
- [10] Sharma SV, Bell DW, Settleman J, Haber D. Epidermal growth factor receptor mutations in lung cancer. *Nat Rev Cancer* 2007;7:169–81.
- [11] Roche Molecular System Inc. cobas EGFR Mutation Test CE-IVD [Package Insert]. Branchburg, NJ, USA: Roche Molecular Systems Inc.; 2011.
- [12] QIAGEN Manchester Ltd. theascreen EGFR RQV PCR Kit Handbook; 2012.

## RESEARCH ARTICLE

# The ALK Inhibitor Ceritinib Overcomes Crizotinib Resistance in Non–Small Cell Lung Cancer

Luc Friboulet<sup>1,2</sup>, Nanxin Li<sup>3</sup>, Ryohei Katayama<sup>1,2,4</sup>, Christian C. Lee<sup>3</sup>, Justin F. Gainor<sup>1,2</sup>, Adam S. Crystal<sup>1,2</sup>, Pierre-Yves Michellys<sup>3</sup>, Mark M. Awad<sup>1,2</sup>, Noriko Yanagitani<sup>5</sup>, Sungjoon Kim<sup>3</sup>, AnneMarie C. Pferdekamper<sup>3</sup>, Jie Li<sup>3</sup>, Shailaja Kasibhatla<sup>3</sup>, Frank Sun<sup>3</sup>, Xiuying Sun<sup>3</sup>, Su Hua<sup>3</sup>, Peter McNamara<sup>3</sup>, Sidra Mahmood<sup>1,2</sup>, Elizabeth L. Lockerman<sup>1,2</sup>, Naoya Fujita<sup>4</sup>, Makoto Nishio<sup>5</sup>, Jennifer L. Harris<sup>3</sup>, Alice T. Shaw<sup>1,2</sup>, and Jeffrey A. Engelman<sup>1,2</sup>

**ABSTRACT**

Non–small cell lung cancers (NSCLC) harboring anaplastic lymphoma kinase (ALK) gene rearrangements invariably develop resistance to the ALK tyrosine kinase inhibitor (TKI) crizotinib. Herein, we report the first preclinical evaluation of the next-generation ALK TKI, ceritinib (LDK378), in the setting of crizotinib resistance. An interrogation of *in vitro* and *in vivo* models of acquired resistance to crizotinib, including cell lines established from biopsies of patients with crizotinib-resistant NSCLC, revealed that ceritinib potently overcomes crizotinib-resistant mutations. In particular, ceritinib effectively inhibits ALK harboring L1196M, G1269A, I1171T, and S1206Y mutations, and a cocrystal structure of ceritinib bound to ALK provides structural bases for this increased potency. However, we observed that ceritinib did not overcome two crizotinib-resistant ALK mutations, G1202R and F1174C, and one of these mutations was identified in 5 of 11 biopsies from patients with acquired resistance to ceritinib. Altogether, our results demonstrate that ceritinib can overcome crizotinib resistance, consistent with clinical data showing marked efficacy of ceritinib in patients with crizotinib-resistant disease.

**SIGNIFICANCE:** The second-generation ALK inhibitor ceritinib can overcome several crizotinib-resistant mutations and is potent against several *in vitro* and *in vivo* laboratory models of acquired resistance to crizotinib. These findings provide the molecular basis for the marked clinical activity of ceritinib in patients with ALK-positive NSCLC with crizotinib-resistant disease. *Cancer Discov*; 4(6); 662–73. ©2014 AACR.

See related commentary by Ramalingam and Khuri, p. 634.

Authors' Affiliations: <sup>1</sup>Massachusetts General Hospital Cancer Center; <sup>2</sup>Department of Medicine, Harvard Medical School, Boston, Massachusetts; <sup>3</sup>Genomics Institute of the Novartis Research Foundation, San Diego, California; <sup>4</sup>Cancer Chemotherapy Center and <sup>5</sup>Cancer Institute Hospital, Japanese Foundation for Cancer Research, Tokyo, Japan

Note: Supplementary data for this article are available at *Cancer Discovery* Online (<http://cancerdiscovery.aacrjournals.org/>).

L. Friboulet, N. Li, and R. Katayama contributed equally to this work.

Corresponding Authors: Jeffrey A. Engelman, Massachusetts General Hospital Cancer Center, CNY 149, 13th Street, Charlestown, MA 02129. Phone: 617-724-7298; Fax: 617-724-9648; E-mail: [jengelman@partners.org](mailto:jengelman@partners.org); Alice T. Shaw, [ashaw1@mgh.harvard.edu](mailto:ashaw1@mgh.harvard.edu); and Jennifer L. Harris, [jharris@gnf.org](mailto:jharris@gnf.org).

doi: 10.1158/2159-8290.CD-13-0846

©2014 American Association for Cancer Research.

## INTRODUCTION

Chromosomal rearrangements of anaplastic lymphoma kinase (*ALK*) are detected in 3% to 7% of non-small cell lung cancers (NSCLC; refs. 1, 2). These rearrangements result in constitutively active *ALK* fusion proteins with potent transforming activity (2, 3). Lung cancers with *ALK* rearrangements are highly sensitive to *ALK* tyrosine kinase inhibition, underscoring the notion that such cancers are addicted to *ALK* kinase activity. On the basis of early-phase studies, the multitargeted tyrosine kinase inhibitor (TKI) crizotinib was approved by the FDA in 2011 to treat patients with advanced NSCLC harboring *ALK* rearrangements (1). However, despite a high response rate of 60% in *ALK*-rearranged NSCLC, most patients develop resistance to crizotinib, typically within 1 to 2 years.

Studies of *ALK*-rearranged lung cancers with acquired resistance to crizotinib have identified *ALK* fusion gene amplification and secondary *ALK* tyrosine kinase (TK) domain mutations in about one third of cases (4–6). To date, seven different acquired resistance mutations have been identified among crizotinib-resistant patients. The most frequently identified secondary mutations are L1196M and G1269A. In addition to these mutations, the 1151T-ins, L1152R, C1156Y, G1202R, and S1206Y mutations have also been detected in crizotinib-resistant cancers (4, 6–10). In approximately one third of crizotinib-resistant tumors, there is evidence of activation of bypass signaling tracts such as EGFR or c-KIT (6, 9). In the remaining one third of crizotinib-resistant tumors, the resistance mechanisms remain to be identified.

Next-generation *ALK* inhibitors with improved potency and selectivity compared with crizotinib have been developed to overcome crizotinib resistance in the clinic. We previously evaluated the ability of several *ALK* TKIs (TAE684, AP26113, ASP3026, and CH5424802) to inhibit *ALK* activity in models harboring different *ALK* secondary mutations (6, 11). These studies revealed variable sensitivity to these *ALK* inhibitors depending on the specific resistance mutation present. For example, the gatekeeper L1196M mutation was sensitive to TAE684, AP26113, and ASP3026, whereas 1151T-ins conferred resistance to all next-generation *ALK* TKIs. Ceritinib is an ATP-competitive, potent, and selective next-generation *ALK* inhibitor (12). The kinase selectivity has been tested in a cellular proliferation assay against 16 different kinases, and aside from *ALK*, no inhibition below 100 nmol/L was observed (12). In the phase I study of ceritinib in *ALK*-positive NSCLC, marked antitumor activity has been observed in both crizotinib-relapsed and crizotinib-naïve patients (13, 14). On the basis of this impressive clinical activity, ceritinib received FDA approval on April 29, 2014.

Herein, we present the first report examining the activity of ceritinib in preclinical models of *ALK*-positive lung cancer with acquired resistance to crizotinib, as well as an early biologic insight into mechanisms of resistance to ceritinib arising in patients.

Table 1. Ceritinib is a potent *ALK* inhibitor

	GI <sub>50</sub> (nmol/L)		
	Crizotinib	Ceritinib	Fold
ALK enzymatic assay	3	0.15	20
H2228	107	3.8	28
H3122	245	6.3	39

NOTE: GI<sub>50</sub> values for *in vitro* *ALK* enzymatic assay or H3122 and H2228 cell survival assay for crizotinib and ceritinib are shown.

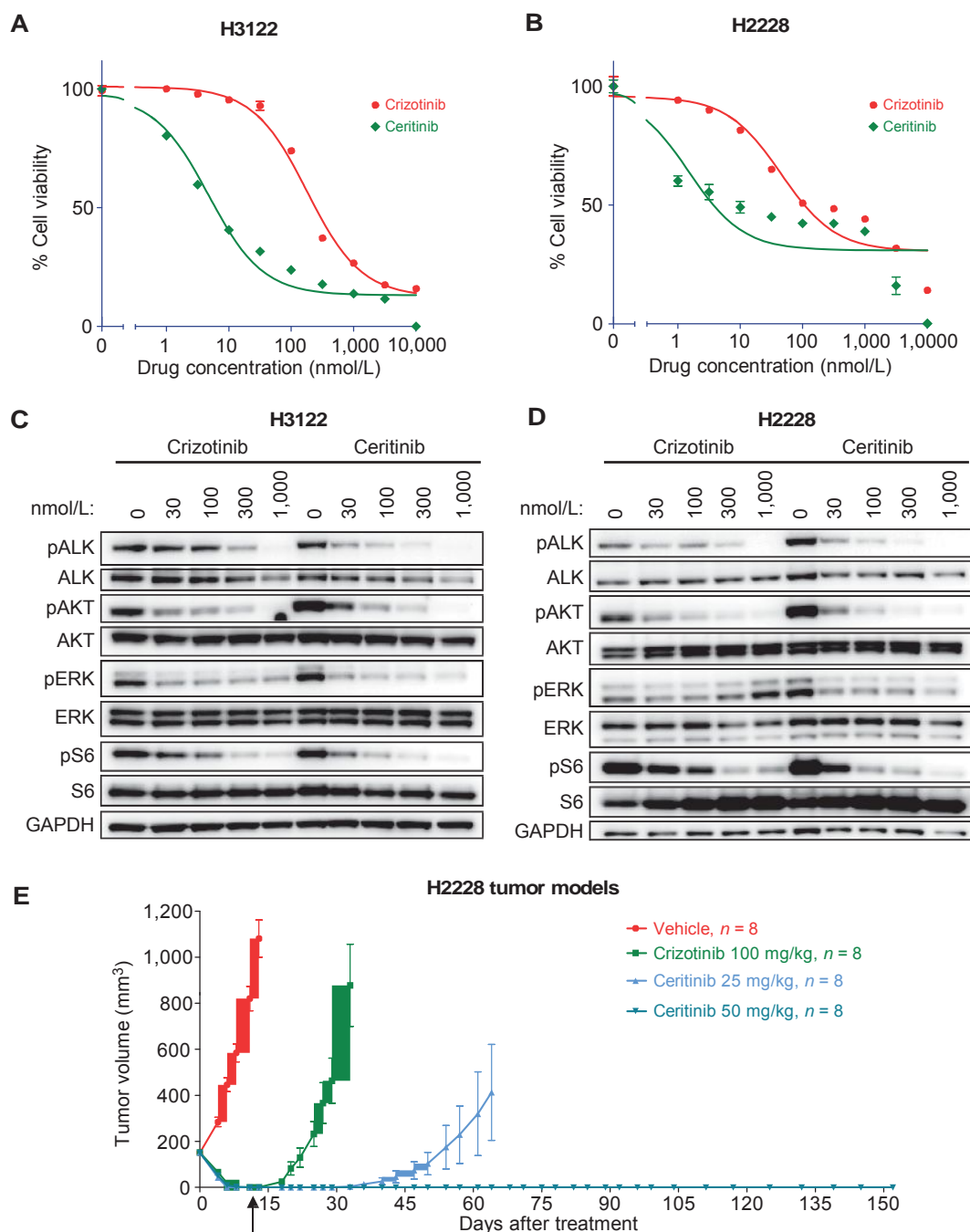
## RESULTS

### Ceritinib Exhibits Potent Activity in Crizotinib-Naïve *ALK*-Positive NSCLC Models

*In vitro* enzymatic studies revealed that ceritinib was approximately 20-fold more potent against *ALK* than crizotinib (Table 1). Similarly, ceritinib was more potent than crizotinib against two *ALK*-rearranged lung cancer cell lines, H3122 and H2228 (Fig. 1A and B, Table 1). Accordingly, ceritinib led to suppression of *ALK* phosphorylation as well as the downstream PI3K–AKT, MEK–ERK, and mTOR signaling pathways at lower doses than crizotinib (Fig. 1C and D).

To further assess the cellular specificity of ceritinib, we determined the GI<sub>50</sub> (concentration needed to reduce the growth of treated cells to half that of untreated cells) of ceritinib against a panel of tumor cell lines bearing different oncogenic drivers. Whereas ceritinib was potent against the two lung cancer cell lines with *ALK* rearrangements, it was not potent against NSCLC or breast cancer cell lines driven by KRAS, EGFR, PI3K, or HER2, with GI<sub>50s</sub> >1 μmol/L (Supplementary Fig. S1A).

We next compared the efficacy of ceritinib and crizotinib *in vivo* using treatment-naïve H2228 xenograft models (Fig. 1E). Tumor-bearing animals were treated with either high-dose crizotinib (100 mg/kg) or ceritinib (25 mg/kg or 50 mg/kg) once daily for 14 days. Both crizotinib (100 mg/kg) and ceritinib (25 and 50 mg/kg) were well tolerated in this study (Supplementary Fig. S1B). As expected, marked tumor regression was observed in all groups during the treatment. After treatment was stopped, the animals were monitored for tumor progression. Although recurrent tumors were detected within 11 days of drug withdrawal in mice treated with crizotinib, mice treated with ceritinib at 50 mg/kg remained in complete remission with no discernible tumor growth for 4 months. In the mice treated with ceritinib at 25 mg/kg, tumor regrowth was observed in 4 of 8 animals after 1 month, whereas complete remission was maintained in the other 4 animals for 4 months. Thus, ceritinib had more durable antitumor activity than crizotinib, even after the drugs were discontinued. It is also worth noting that the exposure of crizotinib at 100 mg/kg is approximately 3-fold to 5-fold greater than the exposures achieved at the human maximum tolerated dose (MTD; 250 mg, twice a day; ref. 15) and that ceritinib at 25 to 50 mg/kg is predicted to be achievable at

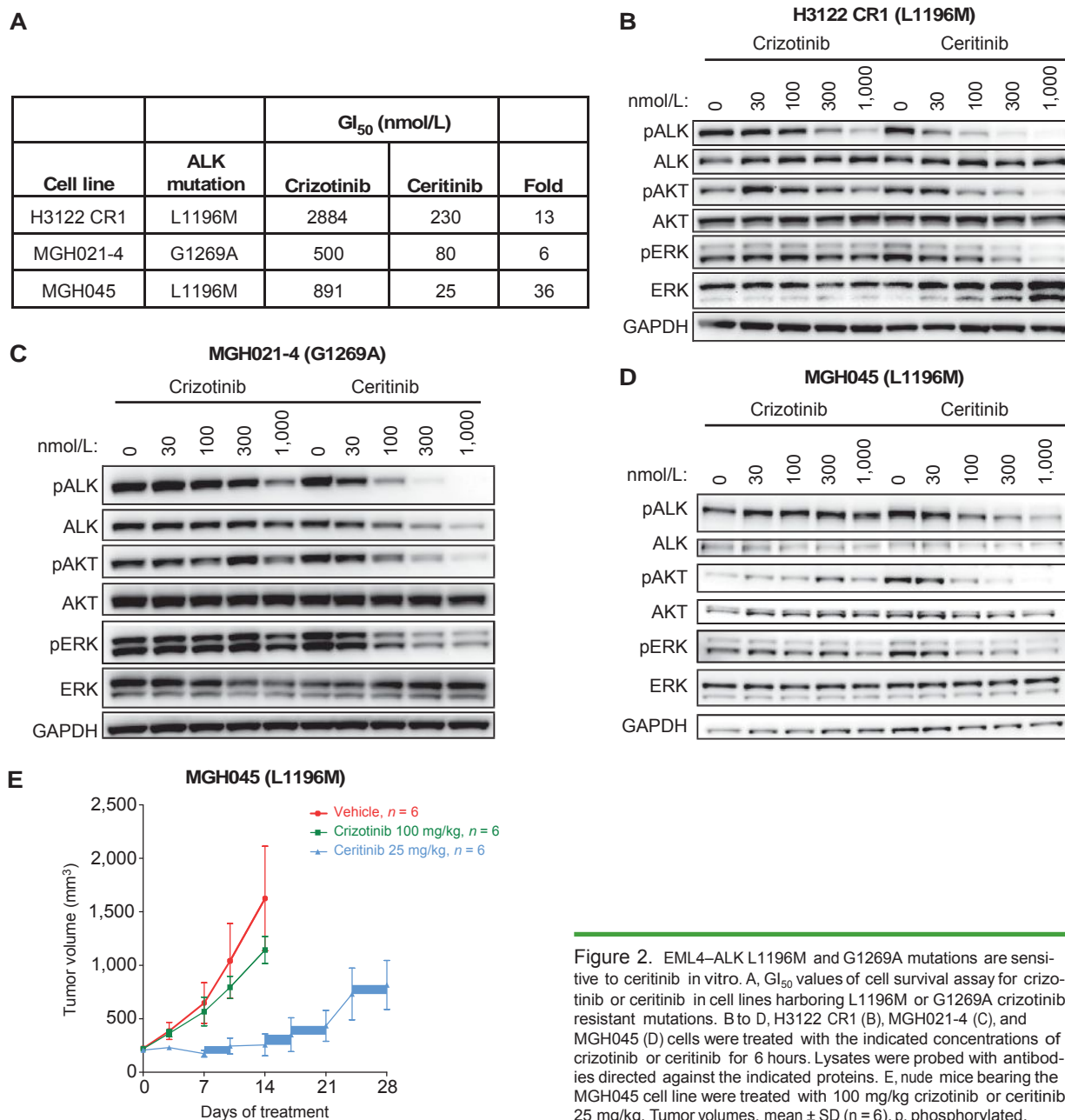


**Figure 1.** Ceritinib is a potent ALK inhibitor in crizotinib-naïve models. A and B, cell survival assay of H3122 (A) and H2228 (B) cells treated with the indicated doses of crizotinib or ceritinib for 72 hours. Cell survival was assayed by CellTiter-Glo. C and D, H3122 (C) and H2228 (D) cells were treated with the indicated concentrations of crizotinib or ceritinib for 6 hours. Lysates were probed with antibodies directed against the specified proteins. E, SCID beige bearing H2228 cells were administered crizotinib or ceritinib orally once daily for 14 days. The arrow indicates when treatments were stopped, and tumor growth was monitored in animals up to 4 months. Tumor volumes, mean  $\pm$  SD ( $n = 8$ ). p, phosphorylated.

the human MTD (750 mg every day). We also evaluated the efficacy of ceritinib in a primary explant model derived from a crizotinib-naïve NSCLC tumor MGH006 (6). Treatment of these mice with 25 mg/kg ceritinib also led to tumor regressions (Supplementary Fig. S1C). Altogether, these data demonstrate that ceritinib is potent against crizotinib-naïve ALK-rearranged cell lines and tumor models *in vivo* and *in vitro*.

### Ceritinib Is Active against Patient-Derived Cell Lines from Crizotinib-Resistant Cancers with and without Resistant Mutations

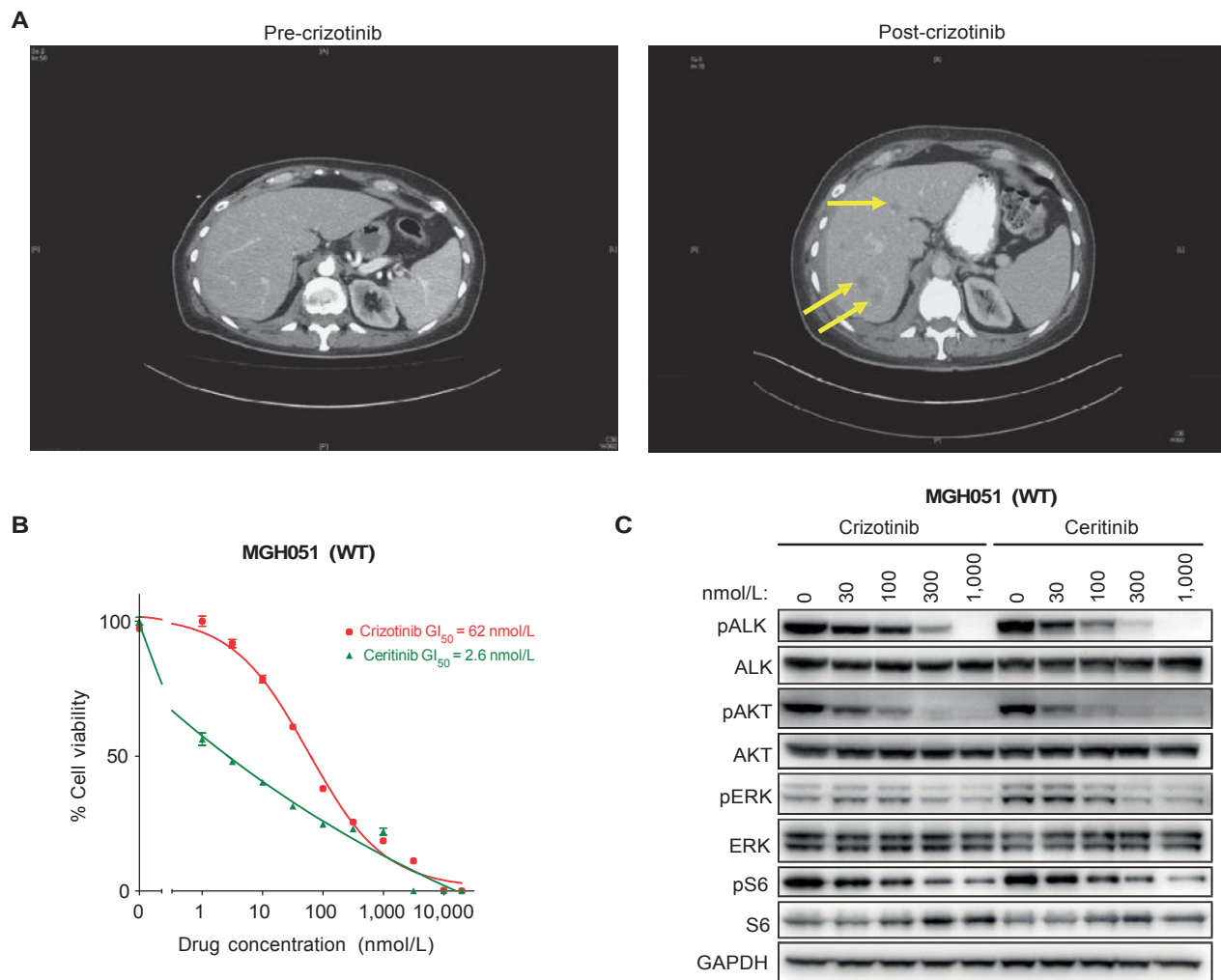
To investigate the activity of ceritinib against crizotinib-resistant mutations, we used crizotinib-resistant cell line models harboring the two most common EML4-ALK



mutations, L1196M and G1269A. We have previously described the H3122 CR1 crizotinib-resistant cell line, which developed resistance *in vitro* by chronic exposure to crizotinib. This cell line harbors both the L1196M *EML4-ALK* gate-keeper mutation and amplification of the *EML4-ALK* allele (11). In addition, we also examined two novel cell lines established from biopsies of patients whose *ALK*-rearranged lung cancers had become resistant to crizotinib in the clinic. These two patient-derived resistant lines, MGH045 and MGH021-4, harbor the L1196M and G1269A mutations, respectively. The MGH021-4 line is a clonal cell line established from MGH021, a tumor harboring both 1151T-ins and G1269A mutations; MGH021-4 cells harbor only the G1269A muta-

tion (5). This clone, therefore, represents an early generation of the patient-derived cell line. The GI<sub>50</sub> values of ceritinib against all of these resistant cell lines were decreased 6-fold to 36-fold compared with crizotinib (Fig. 2A and Supplementary Fig. S2A–S2C). Accordingly, phosphorylation of ALK and downstream ERK and AKT were more effectively suppressed by lower doses of ceritinib compared with crizotinib (Fig. 2B–D).

To further assess the activity of ceritinib against crizotinib-resistant *ALK*-positive tumors *in vivo*, we examined the efficacy of ceritinib against xenografts derived from MGH045 cells that harbor the L1196M resistance mutation. As shown in Fig. 2E, treatment of MGH045 tumor-bearing mice with



**Figure 3.** Ceritinib is active in *ALK* wild-type (WT) crizotinib-resistant cell line. **A**, abdominal computed tomography (CT) images of patient MGH051 before treatment with crizotinib and after 11 weeks of crizotinib. Several new hepatic metastases (yellow arrows) were detectable after crizotinib treatment consistent with disease progression. A repeat biopsy of a hepatic metastasis was performed within 2 weeks of crizotinib discontinuation. **B**, MGH051 cells were treated with the indicated doses of crizotinib or ceritinib for 7 days. After the incubation, the cell survival was assayed by CellTiter-Glo. **C**, MGH051 cells were treated with the indicated concentrations of crizotinib or ceritinib for 24 hours. Lysates were probed with antibodies directed against the indicated proteins.

low-dose ceritinib (25 mg/kg) was more effective than with high-dose crizotinib in controlling tumor growth. These data demonstrate that ceritinib is active against cancers derived from patients with acquired resistance to crizotinib and is more potent than crizotinib against *ALK*-rearranged cancers harboring the L1196M and G1269A resistance mutations.

The ongoing clinical trial of ceritinib demonstrates that crizotinib-resistant *ALK*-positive tumors, including tumors without *ALK* mutation or gene amplification, are responsive to ceritinib treatment (13). This raises the possibility that many of these resistant tumors may develop because of inadequate target suppression. We investigated the efficacy of crizotinib and ceritinib against a crizotinib-resistant *ALK*-positive cell line without *ALK* resistance mutations, MGH051. As shown in Fig. 3A, this cell line was derived from a biopsy of a liver lesion that developed in a patient on

crizotinib. Assessment of the biopsy sample revealed no *ALK* mutations or gene amplification. The cell line derived from the biopsy also did not harbor any *ALK* resistance mutations. This resistant cell line was highly sensitive to ceritinib *in vitro*, and, surprisingly, the MGH051 cell line was also sensitive to crizotinib (Fig. 3B). Accordingly, phosphorylation of *ALK* and downstream *AKT* and *ERK* was efficiently suppressed by crizotinib and ceritinib (Fig. 3C). These data suggest that cancers with acquired resistance to crizotinib without *ALK*-resistant mutations may remain sensitive to *ALK* inhibition (please see “Discussion”).

#### Assessment of Ceritinib Activity against a Panel of *ALK* Mutations

To systematically assess the potency of ceritinib against *ALK* resistance mutations, we used Ba/F3 cells engineered

to express wild-type *EML4-ALK* or one of the nine different resistance mutations. In this system, ceritinib was approximately 10-fold more potent against wild-type *EML4-ALK* than crizotinib. Whereas all these secondary mutations induced crizotinib resistance, ceritinib was potent in inhibiting the growth of Ba/F3 cells expressing four of the resistance mutations, including L1196M, G1269A, S1206Y, and I1171T (Fig. 4A; Supplementary Fig. S3; Supplementary Table S1). However, C1156Y, G1202R, I1151T-ins, L1152R, and F1174C mutations also conferred resistance to ceritinib, although ceritinib was still more potent than crizotinib against these mutations. Thus, the most common crizotinib-resistant mutations were substantially more sensitive to ceritinib than crizotinib, whereas less common resistance mutations conferred resistance to both crizotinib and ceritinib.

### Structural Basis for Increased Potency of Ceritinib against ALK Crizotinib-Resistant Mutations

To glean insights into the structural basis for the ability of ceritinib to maintain activity toward select crizotinib-resistant mutants, the structure of the ALK catalytic domain complexed with ceritinib was determined (Fig. 4B; PDB 4MKC) and compared with the structure of the ALK catalytic domain bound to crizotinib (Fig. 4C; PDB 2XP2; ref. 16). As shown in Fig. 4A, ceritinib retains potency toward the most common G1269A and L1196M crizotinib-resistant mutants. The cocrystal structure reveals that G1269 is situated just proximal to D1270 of the activation loop DFG-motif. Although mutation to Ala in the G1269A mutant would not be predicted to present any steric obstruction to ceritinib binding, it would be predicted to introduce a steric clash to crizotinib binding due to the proximity of the phenyl ring of crizotinib. The Cl moiety of the pyrimidine hinge-binding core of ceritinib is juxtaposed with the L1196 side chain and participates in a hydrophobic interaction with the Leu side chain. In the L1196M mutant, the Cl moiety of ceritinib can interact with Met, which may compensate for the loss of interaction between Cl and the Leu side chain in wild-type ALK. In contrast, introduction of a Met at the gatekeeper position 1196 likely adversely affects crizotinib binding through both steric interference and unfavorable interactions with the 2-amino substituent of the pyridinyl hinge-binding core and the methyl substituent of the alkoxy moiety of crizotinib. These structural findings are in agreement with the increased potency of ceritinib versus crizotinib against these resistance mutations.

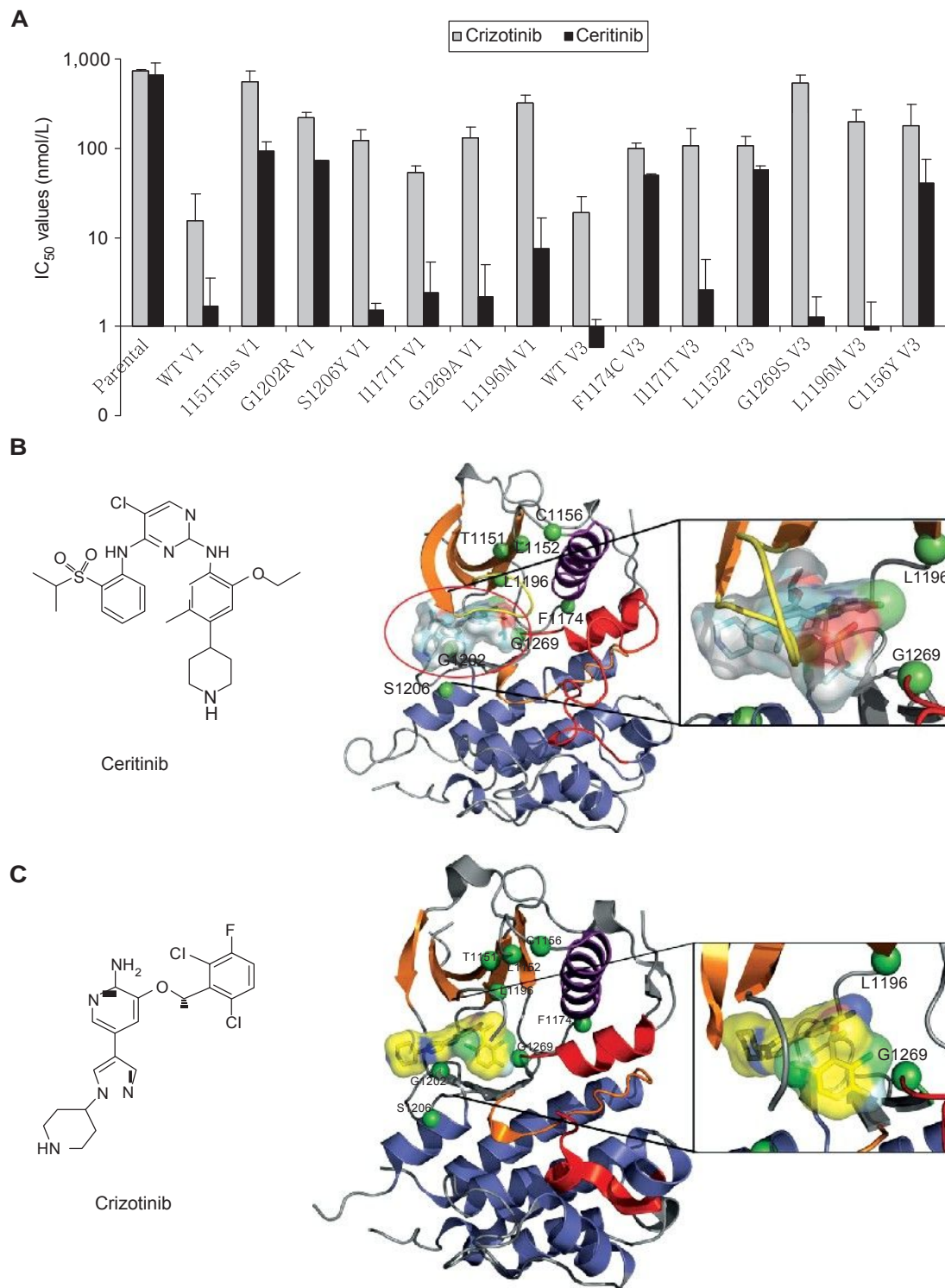
In contrast with G1269A and L1196M mutations, ceritinib is not potent against the G1202R crizotinib-resistant mutation (Fig. 4A). The crystal structure reveals that mutation of G1202 to a larger, bulky, and charged side chain would be incompatible with ceritinib or crizotinib ALK binding due to steric hindrance (6). This steric obstruction leads to a loss in potency as reflected by the shift in  $IC_{50}$  values observed for ceritinib and crizotinib. In contrast with the G1202R mutation, the T1151 insertion, L1152P, C1156Y, and F1174C inhibitor-resistant mutants all map to the N-terminal lobe of the ALK catalytic domain and flank opposing ends of the  $\alpha$ C-helix. The locations of these mutants do not directly contribute to inhibitor binding

in cocrystal structures. Interestingly, positions T1151 and F1174 in ALK have been previously identified as sites of activating gain-of-function mutations in neuroblastoma (17). Although difficult to predict without structural and biochemical analyses of these mutants, T1151 is adjacent to the catalytically important K1150, and insertion at this position, along with the F1174C, L1152P, and C1156Y inhibitor-resistant mutants, likely influences  $\alpha$ C-helix mobility and conformational dynamics of the catalytic domain. Previously reported structures of nonphosphorylated ALK in the apo, ADP, and inhibitor-bound forms suggest the ALK catalytic domain structure possesses a “DFG-in” conformation (18) with a unique activation loop conformation. It is conceivable that these mutations destabilize the ALK conformation and shift the conformational equilibrium toward those that are no longer able to bind the inhibitor. It is also possible that these mutations could decrease the  $K_m$  for ATP, rendering ceritinib/crizotinib a less effective ATP competitive inhibitor.

### Crizotinib-Resistant Tumors Harboring EML4-ALK Wild-Type, I1171T, or C1156Y Mutations Are Sensitive to Ceritinib In Vivo

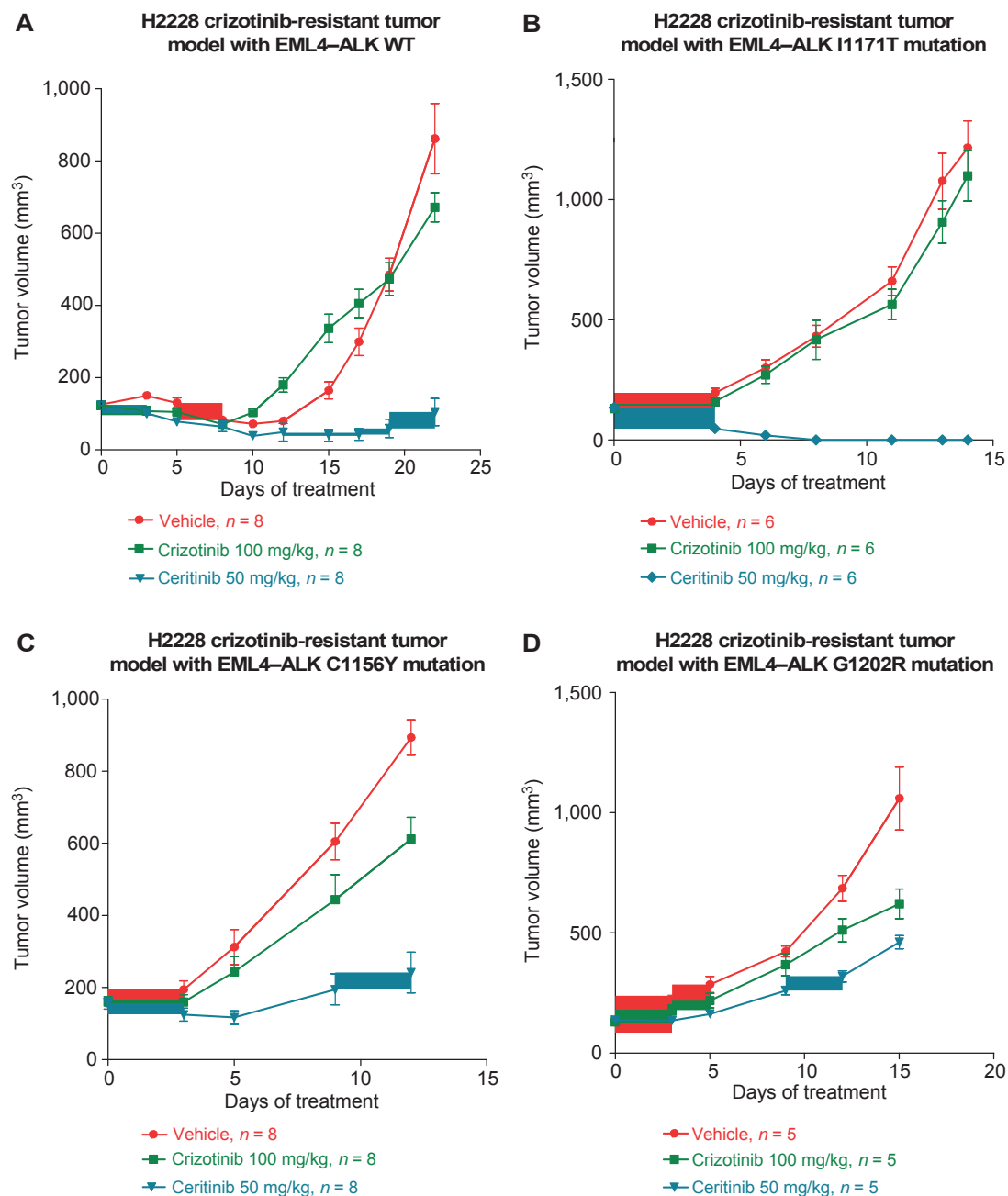
To evaluate the activity of ceritinib against crizotinib-resistant tumors *in vivo*, crizotinib-resistant H2228 xenograft tumors were generated by treatment with escalating doses of crizotinib (from 50 to 100 mg/kg). Tumors that progressed during treatment with 100 mg/kg crizotinib were analyzed for resistance mechanisms. Typical tumor responses and resistance are shown for 3 animals in Supplementary Fig. S4, and are representative of the 80 animals used in this study. To determine mechanisms of resistance to crizotinib, we sequenced the ALK kinase domain of all 80 tumors and identified three distinct resistance mutations in six tumors. The G1202R, C1156Y, and I1171T mutations were detected in three, two, and one resistant tumors, respectively. Of these three mutations, G1202R and C1156Y have been previously reported in patients with NSCLC who relapsed on crizotinib (6, 7). Interestingly, I1171T has not yet been reported from crizotinib-resistant patients but was identified in an *in vitro* mutagenesis screen for resistance mutations (19).

The efficacy of ceritinib was tested against these crizotinib-resistant H2228 xenograft tumor models as well as one of the resistance models that did not harbor a resistance mutation nor *ALK* amplification (data not shown). Although each was resistant to crizotinib at 100 mg/kg, ceritinib suppressed tumor growth in multiple resistance models (Fig. 5A–D). In the wild-type and I1171T resistant models, ceritinib demonstrated impressive antitumor activity, whereas it was less active in the C1156Y-resistant model and was inactive against the G1202R-resistant model. These data are consistent with the Ba/F3 models in which ceritinib was more potent against I1171T than the C1156Y and G1202R mutants (Fig. 4A). The studies shown herein provide evidence that ceritinib can overcome resistance *in vivo*, especially in tumors harboring wild-type, L1196M, or I1171T ALK fusions at a dose that is predicted to be achievable in humans. Of note, it is rather interesting that ceritinib overcame crizotinib resistance in the



**Figure 4.** Ba/F3 models of ALK-crizotinib-resistant mutations. A, IC<sub>50</sub> of ceritinib across different Ba/F3 cell lines expressing wild-type or mutated ALK TK and including parental, IL3-dependent Ba/F3 cells are shown. B and C, ALK-resistant mutations mapped onto ALK/ceritinib (PDB 4MKC; B) and ALK/crizotinib (PDB 2XP2; C) cocrystal structures.  $\beta$ -Strand secondary structural elements of the N-terminal lobe and the  $\alpha$ C-helix of the N-terminal lobe are shown in orange and purple, respectively. Helical structural elements of the C-terminal lobe are shown in blue. Residues of the activation loop (A-loop) and catalytic loop are shown in red and orange, respectively. Residues involved in resistant mutations are depicted as green spheres. Inhibitor molecules are depicted as stick representations with carbons colored yellow and cyan for crizotinib and ceritinib, respectively. Nitrogen is colored dark blue, oxygen is colored red, and chlorine green for both inhibitors. Fluoride is colored white (crizotinib) and sulfur atoms are colored yellow (ceritinib). Transparent surfaces for the inhibitors are displayed. Zoomed-in view boxes for G1269 and L1196 residues are shown. Figures were rendered with MacPymol (The PyMOL Molecular Graphics System, Version 1.4 Schrödinger, LLC).





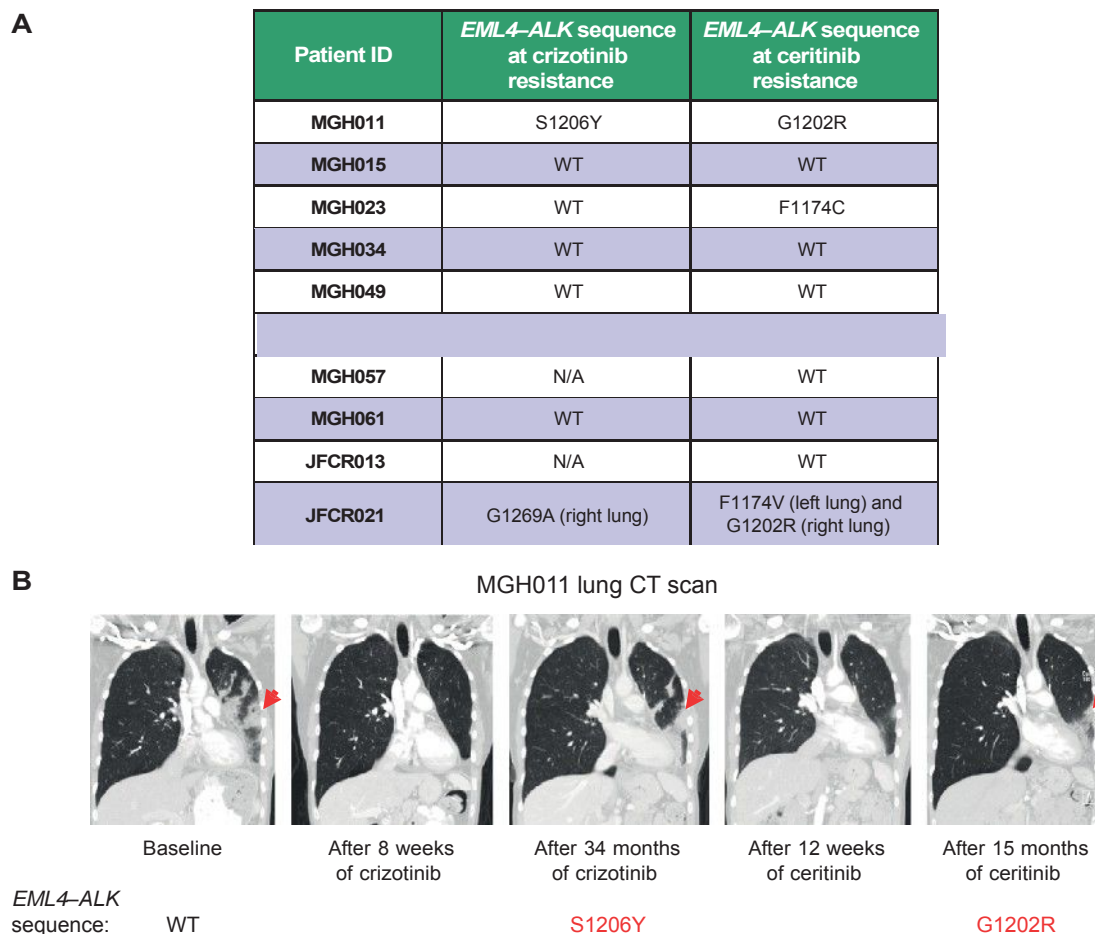
**Figure 5.** EML4-ALK C1156Y, I1171T, G1202R mutations' sensitivity to ceritinib. A to D, SCID beige mice bearing H2228 crizotinib-resistant tumors EML4-ALK wild-type (WT; A), I1171T (B), C1156Y (C), or G1202R (D) were treated with 100 mg/kg crizotinib or 50 mg/kg ceritinib once daily for 12 to 22 days. Tumor volumes, mean  $\pm$  SD ( $n = 5-8$ ).

tumor that did not harbor an *ALK* resistance mutation, as this recapitulates observations in the clinic and with the patient-derived cell line shown in Fig. 3 (please see "Discussion").

#### Acquired Resistance to Ceritinib in Patients

Ceritinib has demonstrated impressive activity in the clinic in crizotinib-resistant patients (13). However, similar to other targeted therapy successes, despite initial and durable

responses, tumors do develop resistance. We have now biopsied 11 cancers with acquired resistance to ceritinib (two of which were from different sites from the same patient). As shown in Fig. 6A, five of these biopsies revealed the development of mutations at either G1202 or F1174 in the ceritinib-resistant cancers. In the patient JFCR021, who had two sites of disease biopsied, two different ceritinib-resistant mutations were identified, underscoring the heterogeneity of resistance mechanisms that can be identified in a single patient (6). Of



**Figure 6.** Ceritinib-resistant tumors acquired mutations at positions G1202 or F1174. A, ALK mutational status in ceritinib-resistant patient tumors before and after ceritinib treatment. B, thoracic computed tomography (CT) images of patient MGH011 during crizotinib or ceritinib treatments. Sites of biopsies (red arrows) revealed the presence of different ALK secondary mutations throughout the treatments. Tumor growth observed during ceritinib treatment is consistent with disease progression. WT, wild-type.

note, 2 of the patients had crizotinib-resistant mutations before enrolling on ceritinib (MGH011; Fig. 6B; and JFCR021) that our laboratory studies suggested would be sensitive to ceritinib. In the ceritinib-resistant cancers, those mutations were no longer detected, but the G1202R mutation emerged (Fig. 6B). These findings are consistent with preclinical studies presented in this article demonstrating the activity of ceritinib against G1269A and S1206Y crizotinib-resistant mutations, and its lack of potency against the G1202R mutation.

## DISCUSSION

Since its approval in the United States in 2011, the ALK inhibitor crizotinib has emerged as a standard of care for patients with advanced NSCLC harboring the *ALK* fusion oncogene. Unfortunately, as has been observed with other targeted therapies, the emergence of resistance has ultimately limited the benefit of this therapy. Next-generation ALK inhibitors (ceritinib, CH5424802, ASP3026, AP26113, and X-396) have been developed with the hope that they may overcome acquired resistance to crizotinib. We previously

reported differential activity of some of these ALK inhibitors depending on the resistance mutations present within the ALK TK domain (6, 11). In an ongoing early-phase clinical study, ceritinib has exhibited dramatic activity in patients with ALK-rearranged NSCLC (13).

In these studies, we find that ceritinib is a more potent ALK inhibitor than crizotinib, and has marked activity in crizotinib-naïve models of *ALK*-positive NSCLC, including H2228, H3122, and Ba/F3 cell lines *in vitro* and MGH006 primary explants *in vivo*. To better characterize the activity of ceritinib in crizotinib resistance, we developed a variety of crizotinib-resistant models, including cell lines derived from biopsies from patients whose cancers had developed resistance to crizotinib in the clinic. These models harbored different resistance mechanisms, including various *ALK* resistance mutations. The activity of ceritinib varied depending on the specific *ALK* resistance mutation. For example, in Ba/F3 models, ceritinib was highly active against L1196M, G1269A, S1206Y, and I1171T *EML4-ALK* mutants, and less active against the less common mutations C1156Y, G1202R, 1151T-ins, L1152P, and F1174C. It is notable that in the phase I

study of ceritinib, five of 19 crizotinib-resistant tumors harbored resistance mutations at residues 1196, 1269, and 1206, with one tumor harboring both G1269A and 1151T-ins. The patients harboring these resistance mutations all exhibited significant tumor shrinkage (13).

Importantly, as has been observed in the clinic, ceritinib showed potent efficacy *in vitro* and *in vivo* against a crizotinib-resistant tumor that did not harbor an *ALK* resistance mutation or gene amplification (Fig. 3B). Interestingly, the patient-derived cell line also retained sensitivity to crizotinib *in vitro*, demonstrating that these cells are still sensitive to *ALK* inhibition. One potential explanation for this finding is that, in the clinic, crizotinib fails to achieve tumor levels that completely inhibit *ALK*, and that tumor cells can survive through modest input from activation of bypass tracks such as EGFR. However, these cells remain sensitive to complete *ALK* inhibition. In the setting of a more potent *ALK* inhibitor, *ALK* is inhibited fully, abrogating the functional role of bypass tracks and leading to the elimination of tumor cells. It is also possible that this patient relapsed on crizotinib because of poor adherence to therapy or due to a stromal contribution. Similar findings were also observed in the H2228 xenograft model that developed resistance to crizotinib *in vivo*, did not develop an *ALK* mutation, and was sensitive to ceritinib (Fig. 5A). These findings may explain, at least in part, the finding that ceritinib is highly active in crizotinib-resistant cancers with or without *ALK* resistance mutations.

The initial interrogation of ceritinib-resistant patient biopsies supports the notion that ceritinib is able to effectively suppress many crizotinib-resistant mutations, but the G1202R and F1174V/C mutants are resistant to ceritinib. It is noteworthy that in two cases, the crizotinib-resistant mutations, S1206Y and G1269A, were no longer observed in the ceritinib-resistant biopsies in which the G1202R mutations were observed (Fig. 6A). This suggests that predominant clones with the S1206Y and G1269A mutations were suppressed by ceritinib, whereas much more rare clones with G1202R mutations were selected by ceritinib. These findings give further support to the notion that there are multiple populations of resistant clones whose emergence is dependent on the selective pressure applied.

Altogether, our *in vitro* and *in vivo* data, including cell line models established from crizotinib-resistant patient samples, demonstrate that the next-generation *ALK* inhibitor ceritinib is active against most crizotinib-resistant tumors. This is consistent with the marked clinical activity of ceritinib in patients with *ALK*-positive NSCLC who progressed on crizotinib. As resistance to ceritinib has already been observed in the clinic, future studies will need to identify mechanisms of resistance to ceritinib other than mutations in the G1202 and F1174 residues to maximize the clinical benefit afforded by next-generation *ALK*-targeted therapies.

## METHODS

### Cell Lines and Reagents

All human lung cancer samples were obtained from patients with informed consent at the Massachusetts General Hospital (MGH) and the Japanese foundation for Cancer Research (JFCR), and all

procedures were conducted under an Institutional Review Board (IRB)-approved protocol. Cells in pleural effusion were collected by centrifugation at  $440 \times g$  for 10 minutes. After red blood cells were lysed with the Red Blood Cell Lysis Solution (BioLegend), cells were grown in ACL-4 (Invitrogen) supplemented with 1% FBS or RPMI-1640 supplemented with 10% FBS and  $1 \times$  Antibiotic-Antimycotic. After the cells started growing stably, clonal cell lines were also established.

H3122, H2228, A549, H460, H1299, HCC827, and H522 cell lines were provided by the Center for Molecular Therapeutics (CMT) at Massachusetts General Hospital (Boston, MA), which performs routine cell line authentication testing by single-nucleotide polymorphism and short-tandem repeat analysis. BT-474, SKBR3, and the *ALK*-positive patient-derived cell lines used in this study are from the Engelman laboratory (Boston, MA) and have been previously tested for mutation status to confirm their authenticity. A549, H460, H1299, HCC827, H522, SKBR3, H2228, H3122, H3122 CR1, and MGH021-4 cell lines were cultured in RPMI-1640 supplemented with 10% FBS. For survival assays, H2228 were cultured in 1% FBS. The MGH045 cell line was cultured in ACL-4 supplemented with 1% FBS, and MGH051 and BT-474 were cultured in DMEM supplemented with 10% FBS.

Mouse myeloma Ba/F3 cells were cultured in DMEM supplemented with 10% FBS with (parental) or without (EML4-*ALK*) IL3 (0.5 ng/mL). cDNAs encoding *EML4-ALK* variant1 or *EML4-ALK* variant3 containing different point mutations were cloned into retroviral expression vectors, and virus was produced as previously described (11). After retroviral infection, Ba/F3 cells were selected in puromycin (0.5  $\mu$ g/mL) for 2 weeks. IL3 was withdrawn from the culture medium for more than 2 weeks before experiments.

Crizotinib was purchased from ChemieTek, and ceritinib was provided by Novartis. Both were dissolved in DMSO for *in vitro* experiments. Ceritinib was formulated in 0.5% methyl cellulose/0.5% Tween 80 and crizotinib in 0.1 N HCl or 0.5% methyl cellulose/0.5% Tween 80 for *in vivo* studies.

### Western Blot Analysis

A total of  $5 \times 10^5$  cells were treated in 6-well plates for 6 hours with the indicated drugs. Cell protein lysates were prepared as previously described (6, 11). Phospho-ERK (T202/Y204), ERK, S6, phospho-S6, phospho-AKT (S473 and T308), AKT, phospho-*ALK* (Y1282/1283), and *ALK* antibodies were obtained from Cell Signaling Technology. GAPDH was purchased from Millipore.

### Survival Assays

Cells (2,000 or 5,000) were plated in triplicate into 96-well plates. Seventy-two hours (48 hours for Ba/F3 cells and 7 days for MGH051) after drug treatments, cells were incubated with a CellTiter-Glo assay reagent (Promega) for 15 minutes, and luminescence was measured with a Centro LB 960 Microplate Luminometer (Berthold Technologies).

### In Vivo Efficacy Study of Ceritinib

SCID beige mice for crizotinib-resistant H2228 xenograft tumor models, nude mice for MGH006 primary explants and MGH045 cells were randomized into groups of 5, 6, or 8 mice with an average tumor volume of approximately 150 mm<sup>3</sup> and received crizotinib or ceritinib daily treatments by oral gavage as indicated in each study. Tumor volumes were determined by using caliper measurements and calculated with the formula (length  $\times$  width  $\times$  height)/2.

### In Vitro Enzymatic Assay

An enzymatic assay for the recombinant *ALK* kinase domain (1066–1459) was conducted using the Caliper mobility shift methodology, using fluorescently labeled peptides as kinase substrates. The

Caliper assay was performed at 30°C for 60 minutes in a total volume of 9  $\mu$ L. The reaction was terminated by the addition of 16  $\mu$ L of stop solution [100 mmol/L HEPES, 5% (v/v) DMSO, 0.1% (v/v) coating reagent, 10 mmol/L EDTA, 0.015% (v/v) Brij 35]. After termination of the reactions, the plates were transferred into the Caliper LabChip 3000 workstation for analysis.

#### Analysis of ALK/Ceritinib and ALK/Crizotinib Costructures

The ALK/ceritinib costructure was determined by the soaking of 2 mmol/L ceritinib into apo crystals grown in 0.2 mol/L sodium acetate trihydrate/20% PEG3350 using protein expressed and purified as previously described (18). The ALK/ceritinib final model determined to 2.0 Å (PDB 4MKC on hold) was superimposed with the coordinates of the ALK/crizotinib costructure (PDB 2XP2) for analyses.

#### Patient Sample Analyses

The patients with ALK-positive NSCLC with acquired ceritinib resistance underwent biopsy of their resistant tumors between January 2011 and September 2013. Standard histopathology was performed to confirm the diagnosis of malignancy as previously described (6). The electronic medical record was reviewed retrospectively to obtain clinical information under an IRB-approved protocol. This study was approved by the IRB of MGH or the Cancer Institute Hospital of JFCR.

#### Disclosure of Potential Conflicts of Interest

M. Nishio has received honoraria from the speakers' bureaus of Pfizer and Chugia Pharmaceutical Co., Ltd. A.T. Shaw is a consultant/advisory board member of Novartis, Pfizer, and ARIAD. J.A. Engelman has received commercial research grants from Novartis and Sanofi-Aventis, and is a consultant/advisory board member of Novartis, Sanofi-Aventis, Chugia Pharmaceutical Co., Ltd., and Ventana Medical Systems, Inc. No potential conflicts of interest were disclosed by the other authors.

#### Authors' Contributions

**Conception and design:** L. Friboulet, N. Li, P.-Y. Michellys, M.M. Awad, A.C. Pferdekamper, S. Kasibhatla, F. Sun, J.L. Harris, A.T. Shaw, J.A. Engelman

**Development of methodology:** L. Friboulet, R. Katayama, M.M. Awad, S. Kim, A.C. Pferdekamper, J. Li, S. Kasibhatla, F. Sun, S. Mahmood, E.L. Lockerman, N. Fujita

**Acquisition of data (provided animals, acquired and managed patients, provided facilities, etc.):** L. Friboulet, R. Katayama, C.C. Lee, J.F. Gainor, A.S. Crystal, N. Yanagitani, A.C. Pferdekamper, F. Sun, X. Sun, S. Hua, P. McNamara, M. Nishio, A.T. Shaw

**Analysis and interpretation of data (e.g., statistical analysis, biostatistics, computational analysis):** L. Friboulet, N. Li, R. Katayama, C.C. Lee, J.F. Gainor, M.M. Awad, N. Yanagitani, A.C. Pferdekamper, S. Kasibhatla, F. Sun, P. McNamara, J.L. Harris, A.T. Shaw, J.A. Engelman

**Writing, review, and/or revision of the manuscript:** L. Friboulet, N. Li, R. Katayama, C.C. Lee, J.F. Gainor, A.S. Crystal, M.M. Awad, J.L. Harris, A.T. Shaw, J.A. Engelman

**Administrative, technical, or material support (i.e., reporting or organizing data, constructing databases):** R. Katayama, A.C. Pferdekamper, S. Mahmood, E.L. Lockerman, N. Fujita, M. Nishio, J.A. Engelman

**Study supervision:** N. Li, S. Kasibhatla, M. Nishio, A.T. Shaw, J.A. Engelman

#### Acknowledgments

The authors thank Thomas Marsilje, Celin Tompkins, and Auzon Steffy for expert technical assistance and input on the studies described in the article; Atsushi Horiike for helping to obtain repeat biopsy samples; and Be a Piece of the Solution and the Evan

Spirito Memorial Foundation for support of lung cancer research at MGH.

#### Grant Support

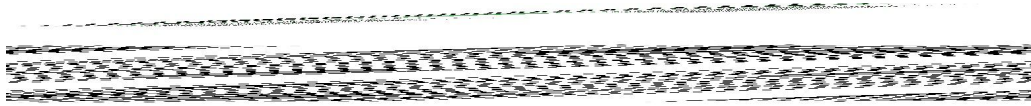
This work was supported by a grant from the NIH (5R01CA164273-02 to A.T. Shaw and J.A. Engelman), by a V Foundation Translational Research Grant (to A.T. Shaw and J.A. Engelman) and by the NIH/National Cancer Institute (R01CA137008 to J.A. Engelman). The study was also supported by a grant from JSPS KAKENHI (25710015 to R. Katayama).

Received November 5, 2013; revised March 12, 2014; accepted March 19, 2014; published OnlineFirst March 27, 2014.

#### REFERENCES

1. Kwak EL, Bang YJ, Camidge DR, Shaw AT, Solomon B, Maki R, et al. Anaplastic lymphoma kinase inhibition in non-small-cell lung cancer. *N Engl J Med* 2010;363:1693-703.
2. Soda M, Choi YL, Enomoto M, Takada S, Yamashita Y, Ishikawa S, et al. Identification of the transforming EML4-ALK fusion gene in non-small-cell lung cancer. *Nature* 2007;448:561-6.
3. Koivunen JP, Mermel C, Zejnullahu K, Murphy C, Lifshits E, Holmes AJ, et al. EML4-ALK fusion gene and efficacy of an ALK kinase inhibitor in lung cancer. *Clin Cancer Res* 2008;14:4275-83.
4. Doebele RC, Pilling AB, Aisner DL, Kutateladze TG, Le AT, Weickhardt AJ, et al. Mechanisms of resistance to crizotinib in patients with ALK gene rearranged non-small cell lung cancer. *Clin Cancer Res* 2012;18:1472-82.
5. Gainor JF, Varghese AM, Ou SH, Kabraji S, Awad MM, Katayama R, et al. ALK rearrangements are mutually exclusive with mutations in EGFR or KRAS: an analysis of 1,683 patients with non-small cell lung cancer. *Clin Cancer Res* 2013;19:4273-81.
6. Katayama R, Shaw AT, Khan TM, Mino-Kenudson M, Solomon BJ, Halmos B, et al. Mechanisms of acquired crizotinib resistance in ALK-rearranged lung Cancers. *Sci Transl Med* 2012;4:120ra117.
7. Choi YL, Soda M, Yamashita Y, Ueno T, Takashima J, Nakajima T, et al. EML4-ALK mutations in lung cancer that confer resistance to ALK inhibitors. *N Engl J Med* 2010;363:1734-9.
8. Lovly CM, Pao W. Escaping ALK inhibition: mechanisms of and strategies to overcome resistance. *Sci Transl Med* 2012;4:120ps122.
9. Sasaki T, Koivunen J, Ogino A, Yanagita M, Nikiforow S, Zheng W, et al. A novel ALK secondary mutation and EGFR signaling cause resistance to ALK kinase inhibitors. *Cancer Res* 2011;71:6051-60.
10. Sasaki T, Okuda K, Zheng W, Butrynski J, Capelletti M, Wang L, et al. The neuroblastoma-associated F1174L ALK mutation causes resistance to an ALK kinase inhibitor in ALK-translocated cancers. *Cancer Res* 2010;70:10038-43.
11. Katayama R, Khan TM, Benes C, Lifshits E, Ebi H, Rivera VM, et al. Therapeutic strategies to overcome crizotinib resistance in non-small cell lung cancers harboring the fusion oncogene EML4-ALK. *Proc Natl Acad Sci U S A* 2011;108:7535-40.
12. Marsilje TH, Pei W, Chen B, Lu W, Uno T, Jin Y, et al. Synthesis, structure-activity relationships, and *in vivo* efficacy of the novel potent and selective anaplastic lymphoma kinase (ALK) inhibitor 5-Chloro-N2-(2-isopropoxy-5-methyl-4-(piperidin-4-yl)phenyl)-N4-(2-(isopropylsulfonyl)phenyl)pyrimidine-2,4-diamine (LDK378) currently in phase 1 and phase 2 clinical trials. *J Med Chem* 2013;56:5675-90.
13. Shaw AT, Kim DW, Mehra R, Tan DS, Felip E, Chow LQ, et al. Ceritinib in ALK-rearranged non-small-cell lung cancer. *N Engl J Med* 2014;370:1189-97.
14. Early Results Promising for LKD378 in ALK-positive NSCLC. *Cancer Discov* 2013;3:OF5.
15. FDA, Center for Drug Evaluation and Research. 2011 Application Number: 202570Orig1s000; Reference ID: 3006911.
16. Cui JJ, Tran-Dube M, Shen H, Nambu M, Kung PP, Pairish M, et al. Structure based drug design of crizotinib (PF-02341066), a potent

- and selective dual inhibitor of mesenchymal-epithelial transition factor (c-MET) kinase and anaplastic lymphoma kinase (ALK). *J Med Chem* 2010;54:6342–63.
17. Chand D, Yamazaki Y, Ruuth K, Schonherr C, Martinsson T, Kogner P, et al. Cell culture and *Drosophila* model systems define three classes of anaplastic lymphoma kinase mutations in neuroblastoma. *Dis Models & Mech* 2013;6:373–82.
  18. Lee CC, Jia Y, Li N, Sun X, Ng K, Ambing E, et al. Crystal structure of the ALK (anaplastic lymphoma kinase) catalytic domain. *Biochem J* 2010;430:425–37.
  19. Zhang S, Wang F, Keats J, Zhu X, Ning Y, Wardwell SD, et al. Crizotinib-resistant mutants of EML4-ALK identified through an accelerated mutagenesis screen. *Chem Biol Drug Des* 2011;78:999–1005.



# The ALK Inhibitor Ceritinib Overcomes Crizotinib Resistance in Non Small Cell Lung Cancer

Luc Friboulet, Nanxin Li, Ryohei Katayama, et al.

*Cancer Discovery* 2014;4:662-673. Published OnlineFirst March 27, 2014.

<b>Updated version</b>	Access the most recent version of this article at: doi: <a href="https://doi.org/10.1158/2159-8290.CD-13-0846">10.1158/2159-8290.CD-13-0846</a>
<b>Supplementary Material</b>	Access the most recent supplemental material at: <a href="http://cancerdiscovery.aacrjournals.org/content/suppl/2014/03/27/2159-8290.CD-13-0846.DC1.html">http://cancerdiscovery.aacrjournals.org/content/suppl/2014/03/27/2159-8290.CD-13-0846.DC1.html</a>

<b>Cited Articles</b>	This article cites by 18 articles, 7 of which you can access for free at: <a href="http://cancerdiscovery.aacrjournals.org/content/4/6/662.full.html#ref-list-1">http://cancerdiscovery.aacrjournals.org/content/4/6/662.full.html#ref-list-1</a>
-----------------------	--

<b>Citing articles</b>	This article has been cited by 10 HighWire-hosted articles. Access the articles at: <a href="http://cancerdiscovery.aacrjournals.org/content/4/6/662.full.html#related-urls">http://cancerdiscovery.aacrjournals.org/content/4/6/662.full.html#related-urls</a>
------------------------	--

<b>E-mail alerts</b>	<a href="#">Sign up to receive free email-alerts</a> related to this article or journal.
----------------------	--

<b>Reprints and Subscriptions</b>	To order reprints of this article or to subscribe to the journal, contact the AACR Publications Department at <a href="mailto:pubs@aacr.org">pubs@aacr.org</a> .
-----------------------------------	--

<b>Permissions</b>	To request permission to re-use all or part of this article, contact the AACR Publications Department at <a href="mailto:permissions@aacr.org">permissions@aacr.org</a> .
--------------------	---